Journal of the European Ceramic Society 42 (2022) 6119–6134

Contents lists available at ScienceDirect

Journal of the European Ceramic Society

journal homepage: www.elsevier.com/locate/jeurceramsoc

Microstructural and residual stress effects on toughening of stoichiometric $BaO.2SiO_2$ glass-ceramics

Simone do Rocio Ferraz Sabino [a,*], Bruno Gabriel Batista Cordeiro [b], Laís Dantas Silva [c], Anderson G.M. Pukasiewicz [d], Edgar Dutra Zanotto [c], Francisco Carlos Serbena [b]

[a] Department of Materials Engineering, State University of Ponta Grossa, Brazil
[b] Department of Physics, State University of Ponta Grossa, Brazil
[c] Department of Materials Engineering, Federal University of São Carlos, Brazil
[d] Federal University of Technology Paraná (UTFPR), Ponta Grossa, Brazil

ARTICLE INFO

Keywords:
Glasses
Glass-ceramics
Barium disilicate
Mechanical properties
Residual stress
Microstructure

ABSTRACT

Barium disilicate ($BaO.2SiO_2$=BS2) glass is one of the few stoichiometric glasses that nucleates internally, homogeneously via thermal treatment. This system has been scarcely assessed in microstructure-property studies. Here we address fracture strength and toughness (K_{IC}) variation as a function of crystallized volume fraction and crystal size, as well as the possible effect of residual stresses (RS) in BS2 glass-ceramics (GCs) by independently varying these two microstructural parameters. K_{IC} increased with spherulite size and crystallized volume fraction. K_{IC} variation with crystallized volume fraction was similar for GCs with different crystal sizes. Combination of the current findings on $BaO.2SiO_2$ (crystals under tensile RS) with previous studies of $Li_2O.2SiO_2$ GCs (compressive RS) indicates that crystallization of a tougher phase – not type of residual stress in the crystals – is the crucial parameter controlling fracture toughness and strength. These findings are quite useful to design novel strong and tough GCs.

1. Introduction

Glass-ceramics (GCs) result from the crystallization of one or more crystalline phases in a glassy matrix. They are defined as "… *inorganic, non-metallic materials prepared by controlled crystallization of glasses* via *different processing methods. They contain at least one type of functional crystalline phase and residual glass. The volume fraction crystallized may vary from ppm to almost 100%*" [1]. GCs normally have mechanical properties superior to those of their parent glasses. Through careful control of their chemical composition and microstructure, several GCs have been designed for domestic and technological applications, such as bioactive implants, dental prostheses, optical devices, and thermal shock resistant materials [2–4]. In GCs, internal residual stresses always arise on the cooling path as a result of the different thermal expansion coefficients (TEC) of the crystalline phases and the residual glass. These residual stresses play an important role in their fracture toughness and strength [5]. Hence, understanding this role and the relationships between microstructure and mechanical properties is of fundamental importance to develop new GCs and novel manufacturing processes, thermal treatments, and applications.

Barium disilicate ($BaO.2SiO_2$ = BS2) glass is one of the very few stoichiometric glass forming systems that undergo internal polymorphic nucleation and crystallization upon heating without nucleating agents [6]. This characteristic allows tight control of the desired microstructure in terms of crystallized volume fraction and crystal size. GCs serve as model materials to shed light on several key materials science and engineering aspects. Studies on their mechanical properties with tight control of the microstructure, such as varying in a controlled manner the crystallized volume fraction and the grain size *independently*, are thus very relevant. However, there are very few published studies addressing such independent variations in crystallinity and crystal size [7–9].

In a previous study, we evaluated the mechanical properties of lithium disilicate (LS2) GCs as a function of the crystallized volume fraction for a constant crystal size - a system where the crystals are subjected to *compressive* residual stresses [8] of approximately 65 MPa. In the BS2 system, however, the residual stresses in the crystals are *tensile*, rendering it a material to further study and understand the role of residual stresses. Therefore, this paper aims to: a) characterize certain

* Corresponding author.
E-mail address: mone.sab@hotmail.com (S.R.F. Sabino).

https://doi.org/10.1016/j.jeurceramsoc.2022.05.073
Received 28 January 2022; Received in revised form 24 May 2022; Accepted 26 May 2022
Available online 2 June 2022

mechanical properties of BS2 GCs by systematically varying the *crystallized volume fraction* for four different *crystal sizes*; b) evaluate the effect of the *type* of internal residual stresses on these mechanical properties.

2. Experimental procedure

2.1. Sample preparation

Two stoichiometric glass batches with 66.7 SiO_2 - 33.3 BaO mol% were prepared from a mixture of barium carbonate ($BaCO_3$) and silica (SiO_2, 99.5% EMSR - Zetasil 2) powders. Two brands of $BaCO_3$ were used: Anidrol (99%), nominated A, and Dinâmica (99.98%), nominated D. These two carbonate brands were used because we ran out of the first (Anidrol) during this four-year research work. The reagents were dried at 120 °C for 12 h, weighed, and homogenized in a roller mill for 12 h. The resulting powder was calcinated at 1350 °C for 36 h in a platinum crucible in a Deltech electrical furnace in air. This procedure was performed to promote the formation of a crystallized mass of barium disilicate by solid-state reaction, which after melting ensures the chemical homogeneity of the glass. Our experience with different stoichiometric glasses, indicates that this is an efficient step to produce a melt with exceptionally good chemical homogeneity, especially when one component (Ba) is much denser than the others. The temperature was then raised to 1550 °C and held for 30 min until complete melting. The obtained melt was poured and pressed between two stainless steel plates. The material was remelted/cast 3 times for homogenization, and the obtained 45 × 20×3 mm^3 blocks were quickly placed in a furnace at 40 °C below the glass transition temperature (T_g ~690 °C) to avoid nucleation and cooled at a 2 °C/min rate to relieve the residual thermal stresses [10].

Samples were cut using a diamond disk in specific dimensions for mechanical testing. Crystallization was performed using a two-stage heat treatment: the first for nucleation and the second for crystal growth. These heat treatments were performed in a small tubular electric furnace with the temperature controlled to within ± 1 °C. The nucleation temperature was 700 °C, and the time was varied to obtain a different number of spherulites. Crystallization temperatures of 800, 785 and 850 °C were used to reach spherulites with mean diameters of approximately 5, 10, 30 and 100 μm, respectively.

To guarantee substantial crystallization, some samples were prepared for a longer time at a higher temperature (940 °C for 720 min), denominated HC_A and HC_D. Table 1 shows the range of temperatures and times used to develop the desired microstructures. For each nucleation condition, the growth period was kept constant to obtain crystals with the same diameter.

After the heat treatments, the samples were ground with silicon carbide sandpaper (360, 600 and 1200 mesh – corresponding to particle sizes of 27 μm, 16 μm, and 6 μm, respectively) and finished with cerium oxide suspension (3 μm granulometry). When it was necessary to reveal the crystals, the polished face was chemically attacked with a solution of 0.2HF/0.6HCl (vol%) for 15 s to promote a contrast between the vitreous matrix and the crystals. The presence of microcracks inside the spherulites and in the glass matrix was clearly confirmed by transmission optical microscopy.

Table 1
Thermal treatment ranges used to produce different microstructures. Glasses A = Anidrol and D = Dinâmica.

Glass	Crystal Diameter	Nucleation		Growth	
	(μm)	T (°C)	t (min)	T (°C)	t (min)
D	**5**	700	30–180	800	25
A	**10**	700	5–90	785	20
A	**30**	700	5–90	850	10
D	**100**	–	–	850	60
A	**HC_A**	700	90	940	720
D	**HC_D**	700	90	940	720

2.2. Microstructural characterization

The glass transition temperature (T_g) was measured using a differential scanning calorimeter (DSC; Setaram Instrumentation, model LABSYS Evo) with a heating rate of 10 °C.min^{-1}. Thermal expansion data were obtained by dilatometry for the BS2 glasses and the HC_A and HC_D samples (700 °C/90 min – 940 °C/12 h); bar samples had dimensions of 4 × 4×25 mm^3. The tests were performed on a Netzsch DIL 402 PC dilatometer in the 30–600 °C temperature range with a 10 °C/min heating rate. The linear thermal expansion coefficient was calculated using linear regression of the thermal expansion curve in the 150–500 °C range.

The crystalline phases were identified by X-ray diffraction (XRD) using a Rigaku Ultima IV X-ray diffractometer in Bragg-Brentano geometry and θ-θ configuration. The XRD diffractograms were obtained using CuK_α radiation (1.54 Å) in the 5°− 80° 2θ range with a 0.02° step and a 10–25 s time step. The diffractometer was equipped with an Anton-Paar furnace, which was used to investigate the evolution of crystallization with temperature and thermal expansion. The phase evolution was studied using a glass powder heated at a 5 °C/min rate and scanned at different temperatures (the temperature was kept constant during scanning) at a continuous speed of 0.5°/min in the 5°− 80° 2θ range and a step size of 0.02°. After cooling to room temperature, the same crystallized powder was submitted to another high-temperature XRD (HT-XRD) analysis for TEC measurement of the crystalline phase. The powder was heated at a 5 °C/min rate, and XRD measurements were performed at 40, 200, 360, 520 and 680 °C in step mode in the 5–80°2θ range with a 0.025–0.03° step size and 20–25 s for each step. To refine the crystalline structure, the Rietveld method was performed using the TOPAS-Academic software [11]. Diffraction peaks were identified using the Inorganic Crystal Structure Database (ICSD).

In BS2 GCs, the crystals are spherulites composed of dendrites with residual glass between them; thus, the crystallized volume fraction significantly differs when measured by XRD or optical microscopy (OM) [12]. We evaluated the spherulite volume fraction (f′) by analyzing several optical micrographs using the ImageJ software. We also evaluated the crystallized volume fraction (f) by XRD. In samples where it was not possible to identify all the crystalline phases, the crystallized volume fraction (f) was evaluated by the ratio of the total area of the diffraction peaks in an XRD to the total area of the XRD trace, including the background in the 2θ interval from 16° to 60°. This was the case for GCs with crystal sizes of 5, 10, 30 and 100 μm with different spherulite volume fractions. For each crystal size, the sample with the highest spherulite volume fraction was selected for the measurement. The amount of residual glass of the HC_A and HC_D GCs was evaluated by XRD of a 50:50 mixture by weight of the GC and α-alumina and by Rietveld refinement.

2.3. Mechanical characterization

The hardness (*H*) and elastic modulus (*E*) of the glass and GC samples were measured by instrumented indentation (UNAT-ASMEC/Zwick/Roell) using a Berkovich diamond tip. The maximum applied load was 400 mN, using the Quasi-Continuous Stiffness Measurement (QCSM) method in a matrix of 5 × 5 indentations. The values of *H* and *E* were calculated following the procedure described by Oliver and Pharr [13], i.e., the averages for each indentation group were taken at the maximum penetration depth.

The strength of the glasses and GCs were determined by the ball on three balls (B3B) test on a universal testing machine (AGS-X 5 kN/Shimadzu). The displacement rate was 500 μm/min with alumina balls (8 mm diameter). The samples were in the form of discs with a diameter of 12 mm and thickness of 1.2 ± 0.1 mm. A total of four samples were

tested for each crystallized volume fraction and crystal size, and the results are the average of these tests.

Fracture strength, σ_S, was calculated according to Danzer et al., [14]:

$$\sigma_S = f(\alpha', \beta, \nu)\frac{F}{t^2}, \quad (1)$$

where F is the load at fracture, t is the sample thickness, and f is a dimensionless factor which depends on the thickness to sample radius ratio ($\alpha' = t/R$), the sphere radius, Ra, the sample radius R ($\beta = R_a/R$), and the Poisson's ratio, ν, of the material tested [14]. The tests were performed at room temperature (25 °C) and 55% air humidity.

The fracture toughness (K_{IC}) was measured by four-point bending tests of bar-shaped 2 × 2×25 mm^3 specimens. All samples were ground in SiC papers of various grit sizes and finished with CeO_2 aqueous suspension. Pre-cracking was performed by a series of 5 N Vickers indentations equally spaced at a distance of 50 μm throughout the specimen width. Under this condition, the indentation-derived radial cracks joined, forming a single crack along the whole sample width [15,16]. Visualization of the crack surface after the fracture tests revealed crack growth before the specimen fracture, even with the highest applied loading rate. The individual indentation median cracks joined into a single crack before the fast fracture of the specimen. Therefore, fracture always occurred from a single large crack. The indentation residual stresses were relieved by treating the samples at 590 °C for 6 h, followed by cooling at a 2 °C/min rate. The tests were performed using a universal testing machine (AGS-X 5 kN, Shimadzu) with a constant displacement rate of 500 μm/min in air (25 °C) and 60% humidity.

K_{IC} was calculated as suggested by Morrell [17]:

$$K_{IC} = 3YF\frac{(l_o - l_i)\sqrt{\alpha}}{2bh^{3/2}(1-\alpha)^{3/2}}, \quad (2)$$

where $Y = [1.9887 - 1.326\alpha - (3.49 - 0.68\alpha + 1.35\alpha^2)\alpha(1-\alpha)]/(1-\alpha)^2$, $\alpha = a/h$, where a is the crack depth, b is the sample width, h is the sample thickness, L_o and L_i are the lower and upper support separation, 20 and 10 mm, respectively, and F is the fracture force [17]. The crack depths were measured after fracture using an optical microscope.

Crack propagation in the microstructure was assessed by etching some GCs in a 0.2HF/0.6HCl (vol%) solution for a few seconds to reveal the spherulites and indenting with a 20 N Vickers indenter. Propagation of the radial cracks was observed by scanning electron microscopy (SEM).

To estimate the amount of crack deflection, mapping profiles of the fractured surfaces tested by four-point bending were evaluated using an optical laser profilometer (Taylor Hobson CCI Lite) with a 50x objective. The scan lines were 250 μm in length and aligned parallel to the crack propagation direction. The crack angles at each point of the line were determined by the profile derivative. The crack deflection angle distributions were calculated as a function of the crystallized volume fraction and crystal size.

Residual stresses were measured using θ–2θ geometry for Synchrotron radiation at room temperature at the XPD beamline of the Brazilian National Synchrotron Light Laboratory (LNLS) using a Mythen 1 K detector. The wavelength was set to 1.5483392 Å, calibrated against a Si standard NIST- 640D. The 2θ-range was scanned from 8° to 80°. The lattice parameters of the GC samples and the stress-free references were refined in the 12°– 80° 2θ-range using the TOPAS-Academic software [11] GCs in powder form were used as stress-free standards. The average residual stresses were calculated as:

$$\overline{\sigma_r} = \frac{E_p}{(1-2\nu_p)}\frac{\Delta V}{3V_o}, \quad (3)$$

where E_p and ν_p are the elastic modulus and Poisson's ratio of the precipitate, respectively, and ΔV is the difference between the unit cell volumes (V_o) of the precipitate under stress and that of the stress-free sample [11].

For all mechanical tests, the crystallized surface layer was removed by polishing prior to testing. The final polishing was performed in aqueous CeO_2 suspension. To relieve the residual stresses generated during polishing, a further heat treatment was performed well below the T_g, at 590 °C, for 2 h, followed by slow cooling to room temperature at a 2 °C/min rate.

The compositions of glasses A and D were measured by an electron probe microanalyzer (EPMA) on a JEOL JXA8230 5-WDS using a 15 kV voltage.

3. Results

3.1. Crystallization and thermal properties

3.1.1. Microstructure

Fig. 1(a)-(d) depict typical optical micrographs of the microstructures obtained for a constant spherulite volume fraction of 35% with different crystal sizes. Spherulites with 30 and 100 μm sizes are *microcracked*. Cracks are observed mainly when two or more crystals join. A few cracks are also observed in the residual glass along the crystal/glass interface contour, as shown later in the insets of Fig. 10(a). These insets show structures and shapes typical of crystals in partially crystallized samples with average spherulitic sizes of 5, 10, 30, and 100 μm, respectively. They have a spherulitic structure composed of dendrites that grow radially with fibrils spreading laterally. The dendritic structure is more evident for the smaller (5 μm) crystals in the inset of Fig. 1 (a). The larger crystals have a more spherical shape, as observed in the inset of Fig. 1(d).

Fig. 2(a)-(c) show microstructures with fixed 30 μm spherulites sizes and 20%, 50% and 70% spherulite volume fractions, respectively, after removal of the crystallized surface layer. Several spherulites have microcracked for all crystallized volume fractions. Also, some microcracks appear in the glass matrix close to the glass/spherulite interfaces.

3.1.2. Crystallization and thermal expansion

Fig. 3(a) shows the differential scanning calorimetry (DSC) curve obtained at the 10 °C/min rate for glass A, where the glass transition temperature ($T_g \approx 695$ °C) and two main exothermic peaks corresponding to the crystallization process are observed; the second event starts at 840 °C (T_{x1}) and appears as a narrow, pronounced exothermic peak, reaching its maximum at 859 °C (T_{P1}). It is also possible to identify a third thermal event, T_{x2}, at 923 °C. These values agree with other DSC characterizations of BS2 glasses [6,10,18] The same thermal events are observed in the DSC curve for the glass D at somewhat higher temperatures; T_g, T_{x1}, T_{P1}, and T_{X2} were 700, 883, 910, and 988 °C, respectively. According to Ramsden and James, the first peak corresponds to the crystallization of the high-temperature monoclinic phase (BS2-H), and the second peak corresponds to the polymorphic transformation of the BS2-H phase into the low-temperature (orthorhombic) phase (BS2-L) [19]. Moulton et al. [20] observed that the second exothermic peak is actually composed of two peaks. The differences in the crystallization temperatures of the two glasses likely reflect small differences in the impurity level and stoichiometry between them.

The thermal expansion coefficients (TECs) of glasses A and D as well as of their respective HC samples are shown in Fig. 3(b). The average TECs are 10.3 × 10^{-6} °C^{-1} for the glass (α_{g_A}) and 13.7 × 10^{-6} °C^{-1} for the HC_A GC (α_{HC_A}). For sample D, the TECs are slightly lower, 9.5 × 10^{-6} °C^{-1} for the glass (α_{g_D}) and 12.4 × 10^{-6} °C^{-1} for the HC_D glass-ceramic (α_{HC_D}). These values are in good agreement with the data in Zanotto [6], who reported TECs of 9.2 × 10^{-6} °C^{-1} for α_g and 12.6 × 10^{-6} °C^{-1} for α_c. These differences are related to the different crystalline phases and crystallized volume fractions between the GCs, as discussed later. For the glasses, these differences are attributed to small differences in chemical composition and impurities and discussed later

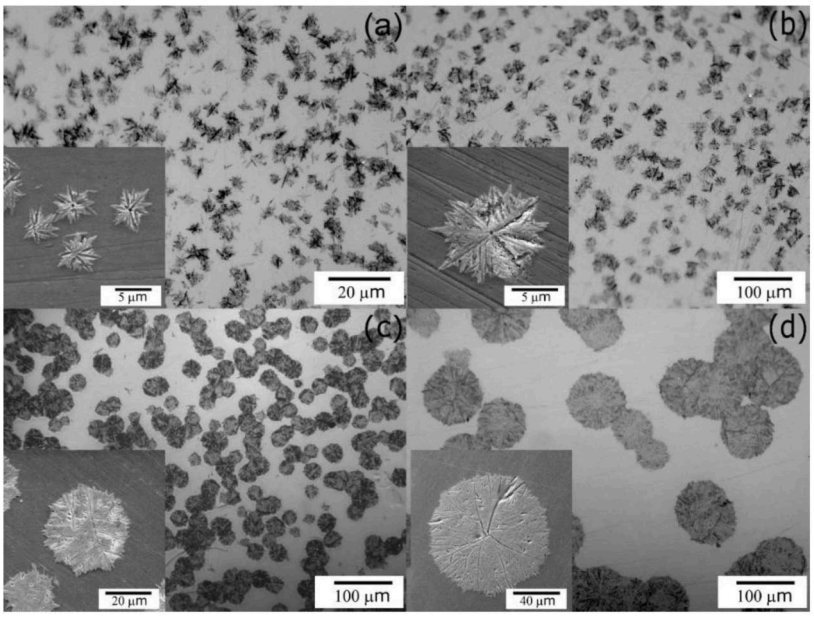

Fig. 1. Optical micrographs showing different spherulite sizes in BS2 GC for a fixed spherulite volume fraction of ~35%. The spherulite diameters are (a) 5, (b) 10, (c) 30, and (d) 100 μm. The insets display SEM micrographs with higher magnification.

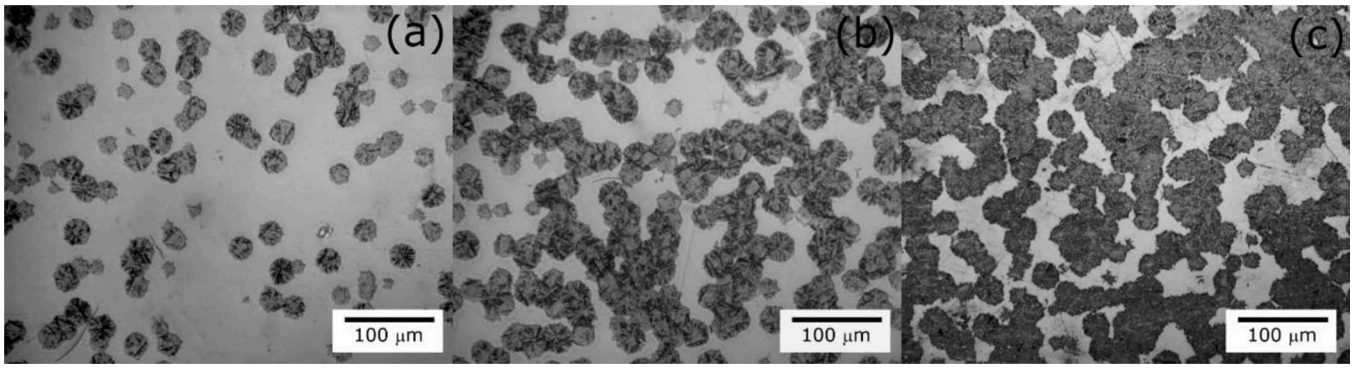

Fig. 2. Crystallized BS2 samples treated for (a) 0 min, (b) 10 min, and (c) 30 min at 700 °C for crystal nucleation and 10 min at 850 °C for crystal growth, corresponding to spherulite volume fractions of 20%, 50%, and 70%, respectively. The spherulite size is ~30 μm.

[21].

3.1.3. Crystalline phases

Fig. 4(a) shows the HT-XRD of glass A powder performed at the onset of the first crystallization peak (840 °C), slightly above it (874 °C), and at the onset of the second crystallization peak (923 °C), in the middle of the peak (947 °C) and slightly above it (965 °C) (see arrows in Fig. 3(a)). Only the BS2-L phase is observed, even at 840 °C, at the onset of the first crystallization peak.

Fig. 4(b) shows the HT-XRD of glass D powder performed at the onset of the first crystallization peak (883 °C), slightly above it (934 °C), at the onset of the second crystallization peak (988 °C) and slightly above the second peak (1050 °C) (see arrows in Fig. 3(a)). Both BS2-L and BS2-H phases are observed. The concentrations determined by Rietveld refinement are 95 vol% BS2-H - 5 vol% BS2-L at 934 °C, and change slightly to 90 vol% BS2-H - 10 vol% BS2-L at 1050 °C.

The XRD patterns of the most crystallized samples for the different crystal sizes and HC samples are shown in Fig. 5(a). XRD experiments of the samples with 5, 10, 30 and 100 μm revealed broad peaks, which did not allow precise identification of the phases. They might be composed of the BS2-L, BS2-H, B3S5 and B5S8 crystalline phases [20,21]. For the HC_A sample, the only crystalline phase was BS2-L. For the HC_D sample, two crystalline phases were observed: BS2-H and B3S5 (see Fig. 5(b) for peak identification of each phase).

Fig. 5(b) shows the XRD and Rietveld refinement results for glass D heat treated at increasing temperatures and longer times. The first diffractogram is of a mixture of HC_D sample and α-alumina in equal proportions in weight for the determination of the glass content. Its composition is 37 vol% BS2-H, 10 vol% B3S5, and 53 vol% residual glass. The second diffractogram represents the HT-XRD of the powder sample after the high-temperature XRD of Fig. 4(b). After heat treatment at all temperatures, the composition was 90 vol% BS2-H and 10 vol% BS2-L. The third diffractogram corresponds to a bulk piece of glass heat treated under the same conditions for crystal nucleation as in sample HC_D (700 °C-90 min), but at a higher temperature for crystal growth (1000 °C-720 min). Its composition is 80 vol% BS2-L and 20 vol% BS2-H. Therefore, the higher the temperature and longer the time, the higher the concentration of the BS2-L phase. Then, a possible evolution of the crystal phases with heat treatment for glass D would be: unidentified phase(s) → BS2-H + B3S5 → BS2-H + BS2-L → BS2-L.

The crystallized volume fractions (f) calculated from XRD traces were compared with the spherulite volume fractions (f') measured by OM. For each group of samples having the same crystal size, the one with the highest spherulite volume fraction was selected for the

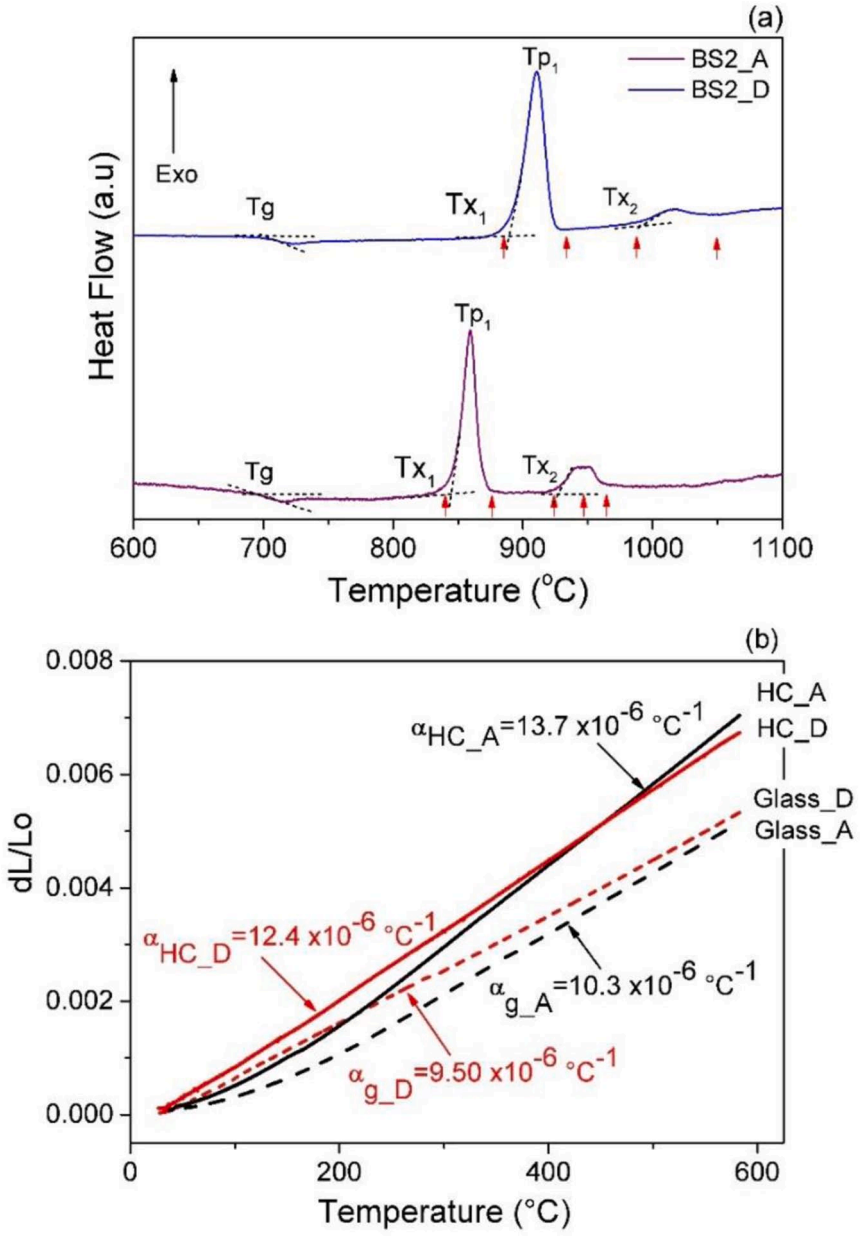

Fig. 3. (a). Differential scanning calorimetry (DSC) traces of BS2 glasses A and D heated to 1100 °C at 10 °C/min, and (b) dilatometric curves for BS2 glasses A and D and HC_A and HC_D (700 °C/90 min-940 °C/12 h) samples. The arrows in Fig. 3(a) indicate the temperatures of the high-temperature XRD experiments (Section 3.1.3).

measurement. As the internal microstructure of the spherulites is the same for samples with the same spherulite size, a simple rule of three allowed estimation of the overall crystallized volume fraction of samples with the same spherulite size. This is a valid assumption, since the heat treatment time and temperature used for crystal growth were the same for crystals with the same spherulite size. The values of f and f from [12] are also plotted. f and f' are different, with $f < f'$. The larger the crystal size, the smaller the difference between them, which suggests that the larger the crystals, the smaller the concentration of residual glass between the dendrites. The amount of residual glass inside the spherulites also depends on the glass batch and crystal growth temperature. The HC_A GC presented 10 vol% residual glass. The HC_D GC had 37 vol% BS2-H, 10 vol% B3S5, and 53 vol% residual glass.

Zanotto and James (1988) experimentally compared the crystallized volume fractions of BS2 GCs measured by XRD and OM, and observed a large discrepancy between the values. After treating two glasses of the same nominal composition at 745 and 760 °C for times ranging from 0 to 20 h, they obtained spherulites from 8 to 17 μm in diameter and observed that the spherulite volume fractions determined by OM from samples treated under the same conditions were much larger than those obtained by XRD. Even for longer times, the crystallized fraction measured by OM was 36% higher than that determined by XRD. This discrepancy, according to those authors, was attributed to the fact that, after long thermal treatments, orthorhombic crystal needles arise from the spherulitic crystals (the first phase to nucleate is monoclinic); therefore, there was a significant amount of glass inside the spherulite, which was difficult to detect by OM. Although the data from Zanotto and James [12] suggest that f saturates at ~64% at 745–760 °C, the HC_A sample in this study reveals that it is possible to obtain even higher crystallized volume fractions.

Crystallization in the spherulites can be calculated from the data in Fig. 6(a) as the f'/f ratio. The data are displayed in Fig. 6(b) as a function

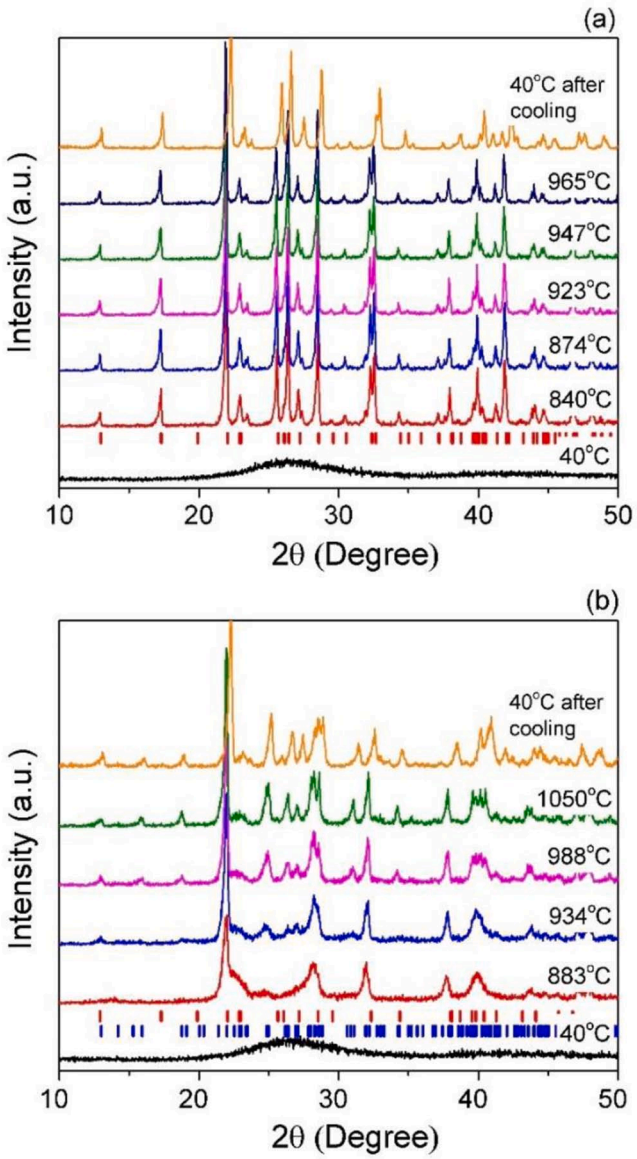

Fig. 4. High-temperature XRD traces of BS2 (a) glass A powder and (b) glass D powder heated at a rate of 5 °C/min and scanned at the indicated temperatures at 0.5°/min (2θ). The temperatures correspond to the onset and slightly above the first crystallization peak, and the onset, in the middle and slightly above the second crystallization peak (arrows in Fig. 3(a)). The marks indicate the diffraction peaks of the BS2-L (red) (ICSD 100313) and BS2-H (blue) (ICSD 100314) phases.

of crystal size. The spherulites with sizes of 5 and 10 μm had the same crystallization, 26%. The 30 μm spherulites, which are from glass A, presented much larger crystallization (68%) than the 100 μm spherulites. The GCs with these spherulites are from glass D, and presented 38% crystallization. Therefore, crystallization increases with increasing spherulite size, but depends on the glass composition.

Chemical analysis by EPMA revealed that the glass A composition is 33.4% BaO, 65.9% SiO_2, 0.1% Al_2O_3, 0.5% Na_2O (mol%), whereas the Glass D composition is 31.6% BaO, 67.3% SiO_2, 0.5% Al_2O_3, 0.4% Na_2O, 0.1% SrO. The precision was 0.1%. The difference in the Al_2O_3 contamination (Glass D = 0.5% and glass A = 0.1%) results in differences in the other components. The differences observed in T_{X1}, T_{P1}, T_{X2}, TEC and crystallization kinetics is attributed to these compositional differences. Alumina is known to increase glass stability, to increase T_X and to reduce thermal expansion. This is consistent with our

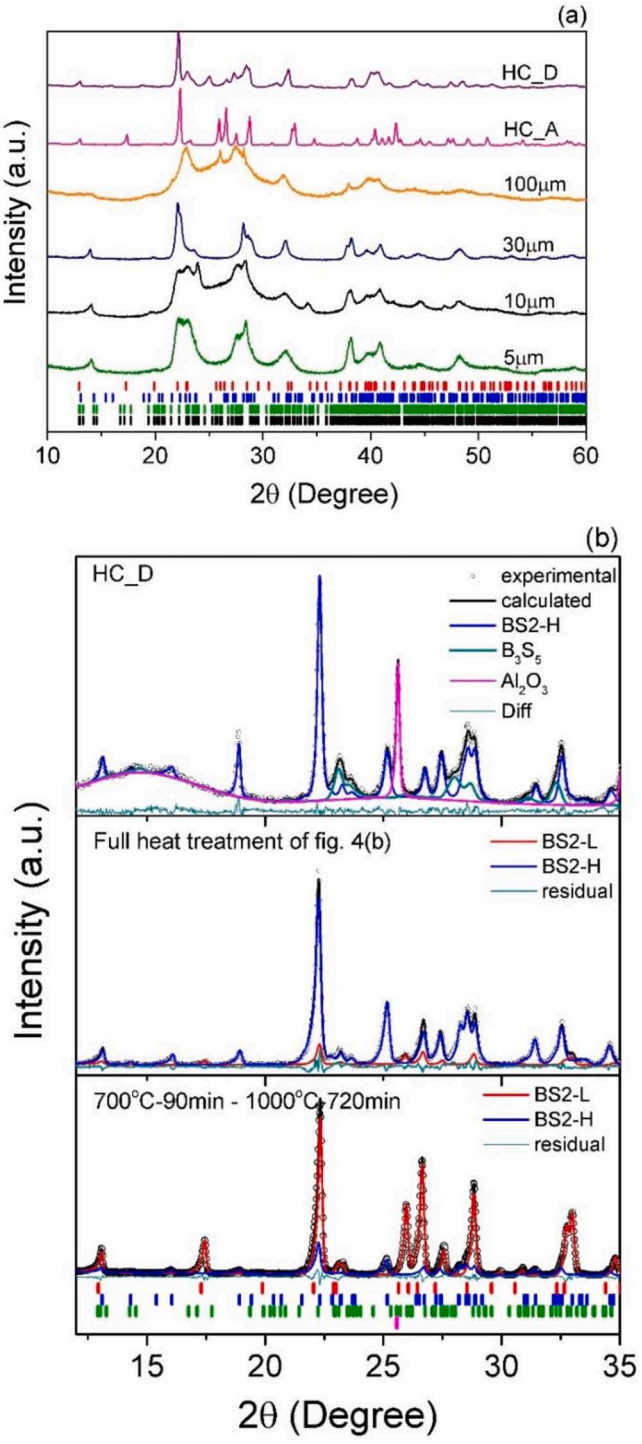

Fig. 5. (a). Diffractograms of BS2 GC treated at 700 °C-90 min for crystal nucleation and at 800 °C-25 min, 785 °C-20 min, 850 °C-10 min, 850 °C-60 min and 940 °C-720 min for crystal growth, corresponding to samples with 5, 10, 30 and 100 μm crystal sizes; as well as HC_A and HC_D samples, (b) Rietveld refinement values of BS2 GCs HC_D + α-alumina (50–50 wt% powder mixture), sample after HT-XRD of Fig. 4(b) (powder), and 700 °C-90 min – 1000 °C-720 min (bulk). The marks indicate the diffraction peaks of the BS2-L (red) (ICSD 100313), BS2-H (blue) (ICSD 100314), B3S5 (green) (ICSD 100312), B5S8 (black) (ICSD 100311) and Al_2O_3 (pink) (ICSD 075479) phases.

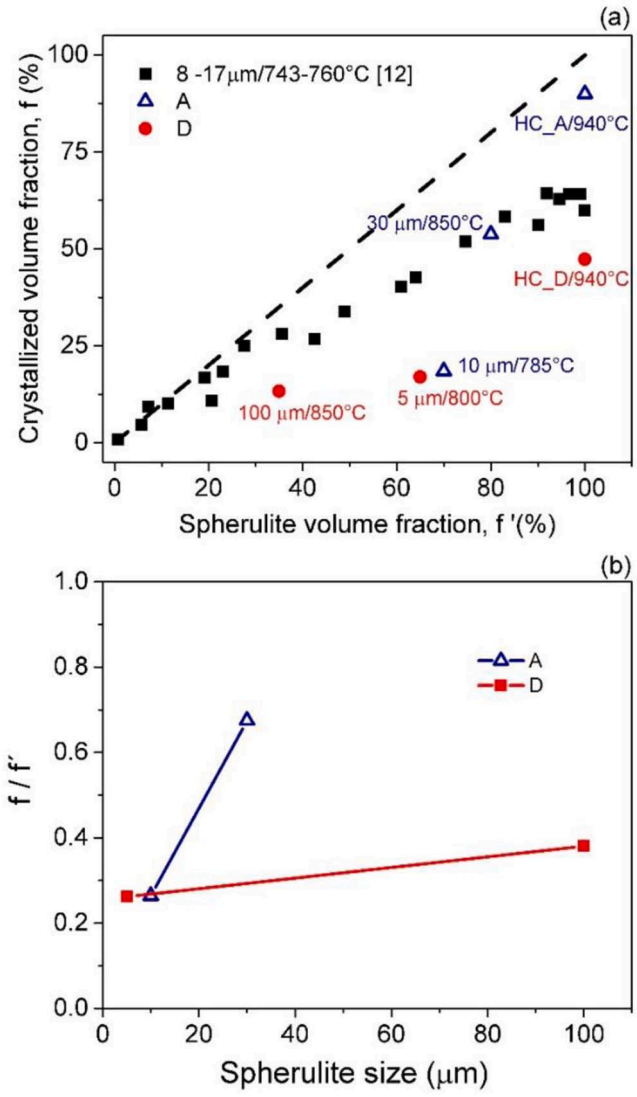

Fig. 6. (a) Crystallized volume fraction measured by XRD (f) compared with the spherulite volume fraction measured by OM (f') [12]. The dashed line indicates $f = f'$. (b) Relative crystallization of each spherulite (f / f) as a function of crystal size.

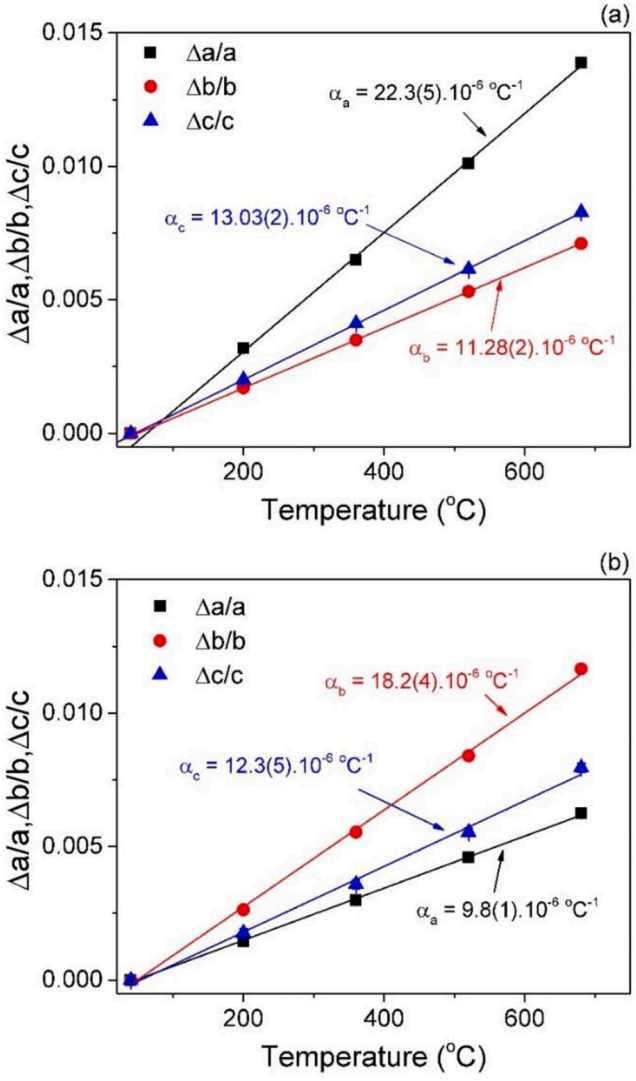

Fig. 7. Thermal expansion of the (a) BS2-L and (b) BS2-H unit cells.

observations, and is an example of the extreme sensitivity of glass crystallization to impurities.

The TEC was also measured by high-temperature XRD (HT-XRD). High-temperature XRD experiments allowed the measurement of the thermal expansion anisotropy of the crystallized phases. The residual stresses depend on the crystal structure, the thermal expansion and elastic constant anisotropies of the crystal phase, T_g and the other properties of the residual glass. Crystal growth in this glass-ceramic is very complex, with spherulites composed of radial dendrites and lateral fibrils with acicular shape, and a residual glass between them. Such microstructure certainly presents anisotropic residual stresses depending on the crystallographic growth direction of the acicular dendrites and fibrils.

A second high-temperature XRD of an HC BS2_A sample was performed just after the HT-XRD of Fig. 4(a), where the sample displayed only the BS2-L phase. Fig. 7(a) displays the TEC of the BS2-L unit cell. The highest TEC was observed for the ***a***-axis (22.3 $\times 10^{-6}$ °C^{-1}), whereas the lowest TEC was found for the ***b***-axis (11.3 $\times 10^{-6}$ °C^{-1}). The average TEC was 15.6(5)x10^{-6} °C^{-1}, which was higher than that measured by dilatometry (13.7 $\times 10^{-6}$ °C^{-1}). These values are in good agreement with the literature; for instance, Rodríguez-López et al. reported a TEC of 12.9 $\times$ 10^{-6} °C^{-1} [22].

A second HT-XRD of an HC BS2_D sample was also performed just after the HT-XRD of Fig. 4(b), where the sample displayed a 90 vol% BS2-H phase and a 10 vol% BS2-L phase. Fig. 7(b) shows the TEC of the BS2-H unit cell. The lowest TEC was observed for the ***a***-axis (9.8 $\times 10^{-6}$ °C^{-1}), whereas the highest TEC was found for the ***b***-axis (18.4 $\times 10^{-6}$ °C^{-1}). The average TEC was 13.4(3)x10^{-6} °C^{-1}.

Kerstan and Russel (2011) measured the TECs of the BS2-H and BS2-L phases by HT-XRD, and obtained BS2-L values of 21.7, 10.6 and 10.8 $\times$ 10^{-6} °C^{-1} for the a-, b- and c-axis, respectively, with an average TEC of 14.4 $\times$ 10^{-6} °C^{-1} [23]. Similar values were measured by Gorelova et al. [24]: 24, 10 and 11 $\times$ 10^{-6} °C^{-1}, with an average TEC of 15 $\times$ 10^{-6} °C^{-1} [24]. The same authors obtained similar TEC values for the BS2-H phase: 21, 8 and 12 $\times$ 10^{-6} °C^{-1} for the a-, b- and c-axis, respectively, with an average TEC of 13.7 $\times$ 10^{-6} °C^{-1} [24].

3.2. Mechanical properties

3.2.1. Hardness and elastic modulus

Fig. 8(a) and (b) show the hardness (H) and elastic modulus (E) values obtained from instrumented indentation as a function of the spherulite volume fraction (f') for different crystal sizes. H decreases slightly with f', from 6.6 GPa for the glass to around 5.6 GPa at $f' = 70\%$.

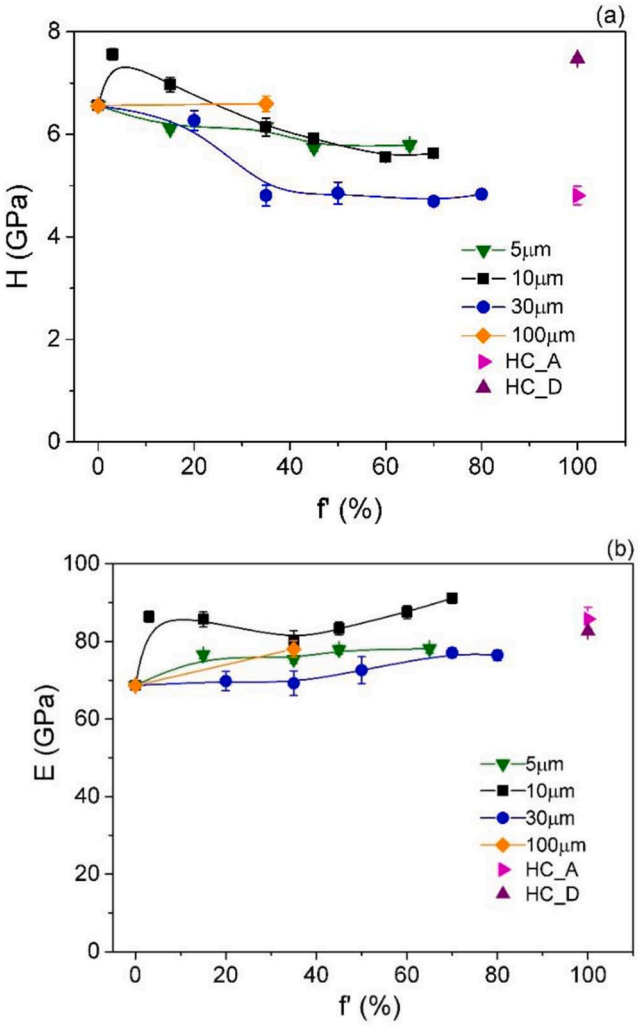

Fig. 8. (a) Hardness (H) and (b) elastic modulus (E) as a function of the spherulite volume fraction, f', measured by instrumented indentation.

The HC_A sample (with only the BS2-L phase) has a lower H value (4.8 GPa) than that of the parent glass, and the H value of the HC_D sample (with 61% BS2-H and 39% B3S5) is higher, 7.5 GPa. No clear trend is observed for dependence on crystal size with constant f'. E increases slightly with f', from 68 GPa for the parent glass to approximately 77 GPa for $f' = 80\%$. The elastic moduli of the HC_A and HC_D samples were $E = 84$ GPa. The same dependence on crystal size observed for H is observed for E, with the highest H and E obtained for samples with a 10 μm crystal size and the lowest values for samples with a 30 μm crystal size. The hardness of BS2-L crystals is ~ 5 in the Mohs scale, being close to that of apatite (hardness = 5) and lower than that of orthoclase ($KALSi_3O_8$, hardness = 6). The measured microhardness using nanoindentation of apatite is 5.4 GPa and that of orthoclase is 6.9 GPa [25]. The BS2 glass hardness measured in this study is 6.6 GPa, close to that of orthoclase. The average H of the GCs is around 5.3 GPa, as shown in Fig. 8(a). Therefore, the decrease in hardness upon crystallization is attributed to the lower H of the BS2-L phase.

3.2.2. Residual stresses

Fig. 9 shows some of the XRD patterns obtained using Synchrotron radiation at room temperature for residual stress measurements. As previously observed, due to the broad peaks, it was not possible to ascribe any known phases to the diffractograms. Therefore, a strategy was adopted to compare the different diffractograms: we determined a unit cell that could fit the different XRD patterns and estimated the

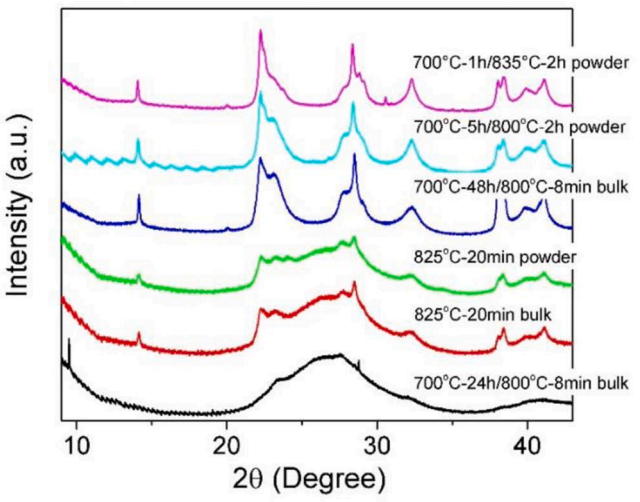

Fig. 9. Diffractograms of the different BS2 GCs used to determine residual stresses. The broad peaks are due to the extremely thin (nanosized) spherulite arms.

average residual stress from the changes in the cell volume. It should be stressed that this "fictive" unit cell does not represent the true unit cell, since more than one phase may be present and the peaks are too broad to be precisely identified. The diffractogram of a sample treated at 700 °C for 1 h and at 835 °C for 2 h was chosen.

Using TOPAS-Academic software, we determined the peak positions and tried to find the unit cell dimensions and space group. Gorelova et al. [24] demonstrated that the atoms in crystalline Ba silicates present chains with two SiO_4 tetrahedra in their repeat units that determine one of the unit-cell parameters (4.560–4.707 Å). Therefore, we looked for a unit cell with one dimension in this range and with the smaller volume possible, similar to H-BS2 ≈ 1200 $Å^3$. The best solution was a monoclinic unit cell with C2 symmetry and the following cell parameters: a = 22.9521 Å, b = 4.7037 Å, c = 12.7062 Å, and $\beta = 62.714°$, with a volume of 1219 $Å^3$. The XRD patterns were fitted using this unit cell. Peak intensities were fitted using the Pawley method. Because a strong correlation with the background was observed, the background of each diffractogram was fitted manually using GSAS [26] and imported in TOPAS to refine the unit cell. The cell volume increased with crystallization time and temperature, which suggests a change in phase composition.

It was not possible to use a single powder sample as a stress-free standard to determine the residual stresses because the unit cell dimensions changed with different heat treatments. The only pair of samples (bulk and powder) with the same heat treatment was the one treated at 825 °C for 20 min. This sample had $f' = 11\%$, $f = 8\%$, and a spherulite diameter of 67 μm. The fitted unit cell volumes were 1216.814 $Å^3$ for the bulk and 1216.846 $Å^3$ for the powder. Assuming $E = 83$ GPa and $\nu = 0.27$, a residual stress of − 2 MPa (very close to zero) is calculated using Eq. (3) This means that microcracking has relieved the residual stresses. This observation is probably valid for all microcracked samples in this study.

3.2.3. Biaxial strength

Fig. 10(a) shows the variation of σ_S with f' and crystal size. The fracture strength increases linearly with increasing f' for the 5 μm and 10 μm crystal sizes. In contrast, for the 30 μm crystal size, σ_S initially decreases with f', whereas above 45%, σ_S increases more rapidly than σ_S for the 5 and 10 μm crystal sizes. The glass strength is 124 ± 6 MPa, whereas for the 80% spherulite volume fraction sample (30 μm), it is 254 ± 4 MPa; an increase of 105%. However, for the GC with a crystal size of 100 μm, the average σ_S is only 67 MPa at $f' = 35\%$, a decrease of 46% in relation to the parent glass. Fig. 10(b) shows the variation of σ_S

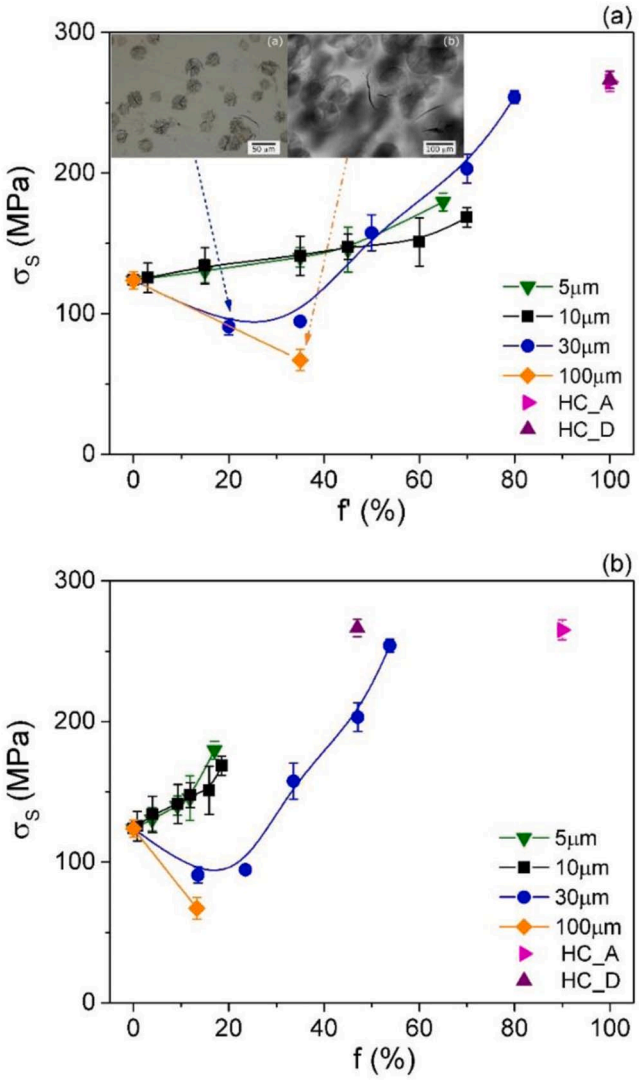

Fig. 10. Biaxial fracture strength (B3B) of BS2 GCs as a function of crystal size (a) and spherulite volume fraction. The insets show the OM analyses of glass-ceramic samples with (a) 30 μm crystals and $f' = 20\%$ and (b) 100 μm crystals and $f' = 35\%$ showing cracks, and (b) crystallized volume fractions in BS2.

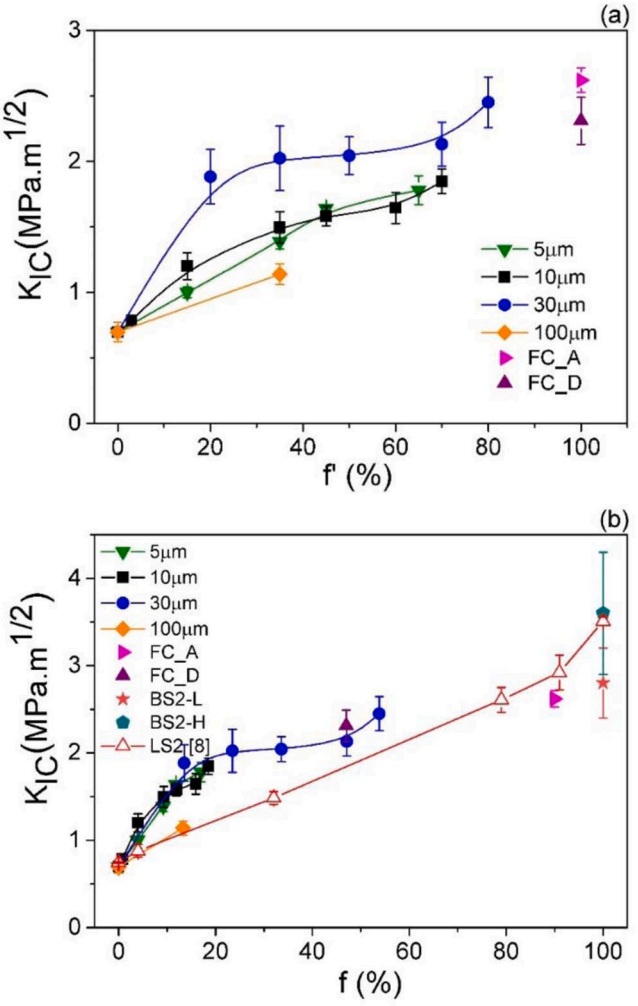

Fig. 11. Fracture toughness as a function of crystal size and (a) spherulite volume fraction; (b) crystallized volume fractions in BS2 GCs. The K_{IC} of the BS2-L and BS2-H phases (*tensile* residual stresses of 40 – 170 MPa) and lithium disilicate GCs from Ref. [8] (*compressive* residual stresses of −65 MPa) are plotted in (b).

with f and crystal size. Samples with spherulite sizes of 5 and 10 μm had higher strength than those with 30 and 100 μm.

Analysis by OM, Fig. 1 and insets of Fig. 10(a), revealed microcracks in the spherulites or in the residual glass surrounding the largest spherulites (30 and 100 μm). Cracks appeared more frequently close to groups of 3 or 4 overlapping spherulites. These cracks were produced by the thermal residual stresses, and certainly decreased the strength of these GCs. No cracks were observed for GCs containing 5 and 10 μm crystals. The crack morphology indicates *tensile* residual stresses in the spherulites [5].

3.2.4. Fracture toughness

Fig. 11(a) shows the variation of K_{IC} with f' and crystal size. For the parent glasses A and D, the K_{IC} values were 0.7 ± 0.1 and 0.74 ± 0.06 MPa.m$^{1/2}$, respectively, which are typical for silicate glasses. Crystallization increased K_{IC} up to 2.5 ± 0.2 MPa.m$^{1/2}$ for the most crystallized sample having 30 μm crystals. The K_{IC} increases rapidly at low f' and, after 30%, the increase is less pronounced. Samples with larger crystal sizes have a higher K_{IC}. This behavior is similar to that observed in a previous study conducted with lithium silicate GCs [8].

Fig. 11(b) shows the variation of K_{IC} with the crystallized volume fraction, f. Since the relation between f and f' was measured for different crystal sizes, a proportional relation was assumed between f and f' for other GCs with the same spherulite size. It is interesting to observe that for the true crystallized fraction measured by XRD, K_{IC} does not depend on crystal size; it depends only on f.

We also plotted the estimated value of K_{IC} for the BS2-L and BS2-H phases from data of the HC_A and HC_D samples. For these calculations, we assumed that the strain energy release rates (G_C) of the glass-ceramic result from a rule of mixing the strain energy release rates of the residual glass and the crystalline phase. A condition of *plane strain* was assumed. We considered Poisson's ratios of 0.274 for the glass [27] and 0.25 for the crystalline phases [28], and that the E and G_C of the BS2-H and B3S5 phases were the same. The elastic moduli of the BS2-L (from HC_A GC) and BS2-H (from HC_D GC) phases were calculated from a rule of mixtures from the measured E and f of each GC and the glass. They are 88 GPa for BS2-L and 98 GPa for BS2-H. The calculated strain energy release rates are 7 ± 1 J.m^{-2} for the glass, 90 ± 20 J.m^{-2} for BS2-L, and 120 ± 40 J.m^{-2} for BS2-H; hence, the estimated K_{IC} values are 2.8 ± 0.4 MPa.m$^{1/2}$ for BS2-L and 3.5 ± 0.6 MPa.m$^{1/2}$ for BS2-H (please recall that the crystals in the GCs are under *tensile* residual stresses of 40–170 MPa). The K_{IC} of the BS2-H phase is 35% higher than that of the BS2-L phase. The BS2-H also has a higher H than the BS2-L phase. Hence, for applications where mechanical properties are important,

crystallization of the BS2-H phase is likely desirable over the BS2-L phase.

Additionally, Fig. 11(b) shows the variation in toughness of lithium disilicate GCs as a function of f for a constant crystal size of 12 μm [8], which have an average *compressive* residual stress of − 65 MPa in the crystals, which is within the stress level range observed for the BS2 GCs with spherulites with sizes of 5 and 10 μm. In both cases – tensile (BS2) or compressive (LS2) residual stresses – K_{IC} increases with the crystallized volume fraction, reaching values of ~3.5 MPa.m$^{1/2}$, indicating that the stress type is *not* important, and the key microstructural feature for enhancing K_{IC} in these GCs is the *crystallized volume fraction* of a tougher phase. The fracture toughness of the BS2 GCs is higher than that of the LS2 GCs for $f < 40\%$. This may be caused by the acicular shape of the dendrites inside the spherulites, which increases toughness more than the round ellipsoidal crystals of the LS2 GCs [29].

Fig. 12(a-c) show the different mechanisms of crack toughening operating in the BS2 GCs. Most crack deflection occurs inside the spherulites, with cracks propagating straight in the glass matrix. Inside the spherulites, the cracks propagate along the dendritic crystal/residual glass interface, as displayed in Fig. 12(b). Crack bridging with ligaments inside the spherulites is observed in Fig. 12(a), which indicates that crack trapping is a possible toughening mechanism in the BS2 GCs. The cracks tend to deviate from the spherulites, as shown in Fig. 12(c).

3.2.4.1. Topography of the fracture surfaces. The surface profiles of the fracture surfaces were measured using an optical laser profilometer. They revealed that as f increases, crack deflection becomes more significant. This is observed in Fig. 13(a-d) for representative crack profiles for different f and crystal sizes. Images of the fracture surfaces are shown in Figs. S1 (Supplementary Material).

The distribution of the crack deflection angles and the angular cumulative distributions were calculated for all samples (Figs. S2 (a)-(d) and Figs. S3 (a)-(d), respectively). For the GCs, increasingly sharper angles were observed with increasing the crystallized fraction. The distributions are unimodal, and the median increases with the crystallized volume fraction, from **1.2**° for the glassy sample to **24.4**° for the HC sample.

4. Discussion

4.1. Mechanical properties

4.1.1. Residual stresses

As previously mentioned, the BS2 spherulites contain some residual glass, and the crystallized fraction within each spherulite increases with increasing the spherulite radius. Due to the small crystallite size inside the spherulites and very broad XRD peaks, we could not identify the crystal phases, but they are likely BS2-L, BS2-H, and some Ba-rich phases, such as B5S8 and B3S5. In the presence of these Ba-rich phases, the residual glass inside the spherulites would be depleted in Ba and richer in Si, which would lower the TEC of the residual glass and increase the residual stresses, σ_P, in the crystals.

For simplicity, we will calculate σ_P assuming that the crystalline phases in the spherulites are BS2-L or BS2-H. We will estimate the σ_P for a low f, which will give the highest bound for the residual stresses. Due to the force balance in the crystals and glass, as f increases, the stresses decrease in the spherulites and increase in the residual glass.

Selsing [30] proposed that the residual stress in the precipitates caused by the TEC mismatch between the crystal and the glass matrix, for low crystallized volume fractions, in the isotropic case is given by:

$$\sigma_P = \frac{\Delta\alpha.\Delta T}{K_e}, \tag{4}$$

where $K_e = (1 + \nu_m)/2E_m + (1 - 2\nu_P)/E_P$, Δα is the TEC difference between the precipitate and the glass matrix, ΔT is the temperature difference between T_g and room temperature, E and ν are the elastic modulus and Poisson's ratio, respectively, and p and m refer to the precipitate and matrix, respectively.

For the residual glass, $\alpha_g = 10.3 \times 10^{-6}$ °C^{-1}, $E_g = 68$ GPa, and $\nu_g = 0.274$; for BS2-L, $\alpha_P = 15.6 \times 10^{-6}$ °C^{-1}, $E_P = 88$ GPa, and $\nu_g = 0.25$; for BS2-H, $\alpha_P = 13.4 \times 10^{-6}$ °C^{-1}, $E_P = 98$ GPa, and $\nu_g = 0.25$, as measured in this study. The TEC (α_S), elastic modulus (E_S), and Poisson's ratio (ν_S) of the spherulites were calculated assuming a rule of mixtures between the crystal phases (BS2-L or BS2-H) according to the data of Fig. 6(b):

$$\begin{aligned} \alpha_S &= \frac{f}{f'}\alpha_c + \left(1 - \frac{f}{f'}\right)\alpha_g, \\ E_S &= \frac{f}{f'}E_P + \left(1 - \frac{f}{f'}\right)E_g, \\ \nu_S &= \frac{f}{f'}\nu_P + \left(1 - \frac{f}{f'}\right)\nu_g. \end{aligned} \tag{5}$$

If BS2-L is the crystalline phase, the residual stresses in the spherulites are in the 60–170 MPa range; whereas for the BS2-H phase, they are in the 40–100 MPa range, for the different spherulite sizes. The highest and lowest σ_P values are found for the 30 μm and 10 μm spherulites, respectively. Therefore, the predicted average residual stresses are *tensile* and in the 40–170 MPa range, depending on the crystalline phase.

We can also estimate the residual stress from the critical radius for

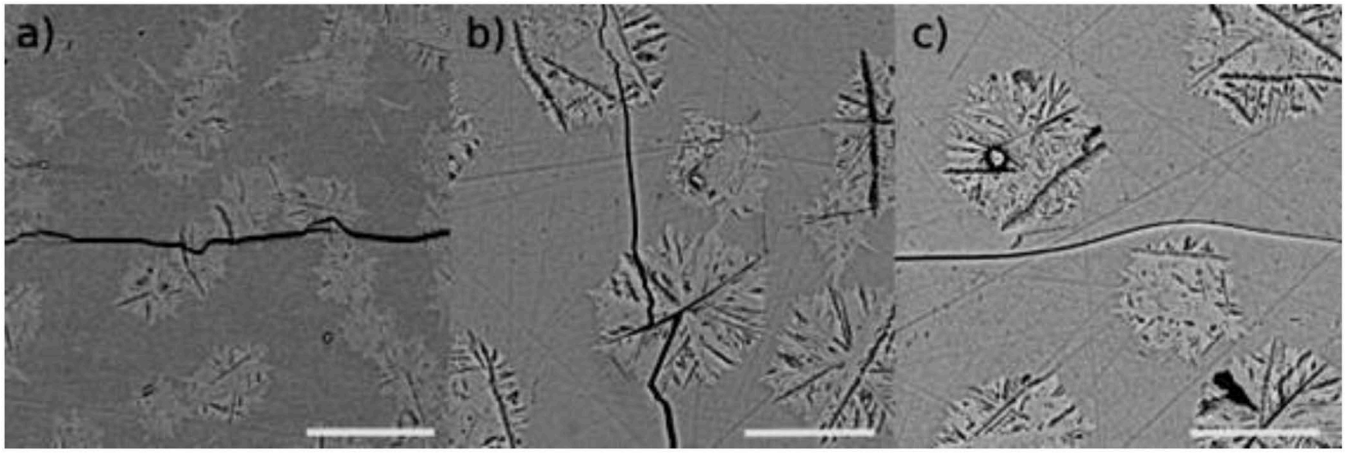

Fig. 12. SEM micrographs using backscattered electrons showing radial cracks emanating from 20 N Vickers indentations in GCs with: a) $f = 35\%$ and spherulite size of 10 μm, and (b-c) $f = 35\%$ and spherulite size of 30 μm. The calibration bars are 20 μm.

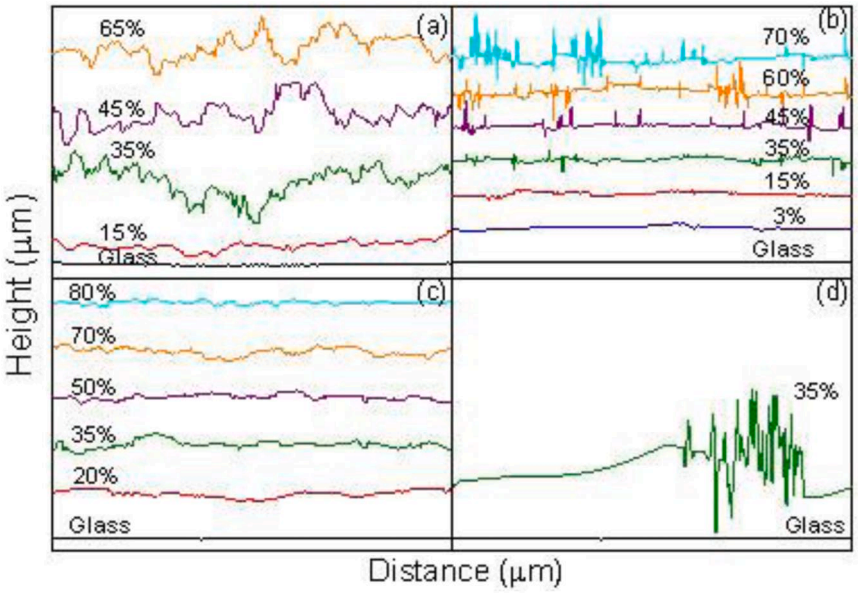

Fig. 13. Representative fracture profiles for the different spherulite volume fractions for (a) 5, (b) 10, (c) 30 and (d) 100 μm crystal sizes.

spontaneous microcracking. Spontaneous microcracking of the spherulite/glass matrix occurs if the spherulite radius is larger than a critical radius, R_C [5,30–32].

$$R_C = \frac{2\gamma_S}{K_c \sigma_P^2}, \tag{6}$$

where γ_S is the fracture energy of the spherulite/glass that is equal to $K_{IC}^2/2E'$, where $E' = E/(1-\nu^2)$ for the plane strain. In Section 3.2.4, the calculated strain energy release rates were 7 J.m^{-2} for glass, 90 J.m^{-2} for BS2-L, and 120 ± 40 J.m^{-2} for BS2-H. As $2\gamma_S = G_C$, then $\gamma_S^{glass} = 3.5$ J.m^{-2}, $\gamma_S^{BS2\text{-}L} = 45$ J.m^{-2}, and $\gamma_S^{BS2\text{-}H} = 60$ J.m^{-2}. Assuming a rule of mixtures for the fracture energy of the spherulite: $\gamma_S^{spherulite} = 34$ J.m^{-2} and $\gamma_S^{spherulite} = 45$ J.m^{-2} for BS2-L and BS2-H, respectively - the main crystalline phases for GCs with low f.

If microcracking occurs in the precipitates, critical radii of 151 and 567 μm are calculated using Eq. (6) for the BS2-L and BS2-H phases, respectively. On the other hand, if microcracking occurs in the glass matrix surrounding the spherulites, critical radii of 16 and 44 μm are calculated for the BS2-L and BS2-H phases, respectively. In this way, the predicted critical radius for microcracking of the glass matrix is in good agreement with the experimental observations, since two or more attached spherulites can act as a microcracking source. For the case of microcracking in the spherulites, the calculated R_C is much larger than the experimental spherulite radius. As mentioned earlier, one possible source of such discrepancy is the precipitation of Ba-rich phases, which would lead to a silica-rich residual glass, lowering its TEC and increasing σ_P. Another possible source of discrepancy is thermal expansion anisotropy. As the spherulites are composed of axially growing needle-shaped crystals, the preferential growth direction might be one of the high TECs. If we assume the spherulite TEC is equal to the highest TEC of the unit cell, according to Fig. 7(a-b), critical radii of 30 and 87 μm are obtained for BS2-L and BS2-H, respectively. These calculated RCs agree with the experimental observations.

The residual stress state in BS2 GCs is quite complex. There are stresses in the glass matrix, in the spherulites (average residual stresses calculated in this article), in the internal dendrite arms, and in the residual glass inside the spherulites. XRD measurements would provide a macro view of the residual stresses in the internal dendrites, however, these dendrites are far too small (too broad XRD peaks) for a reliable measurement. Despite this problem, we were able to determine the (null) residual stress in a sample having large micro cracked spherulites. Hence, we only calculated the average residual stresses in the spherulites, which are *tensile* in the 40–170 MPa range. They decrease with higher f and f for a constant spherulite size. Although the residual stresses should not depend directly on the crystal radius, as predicted by the Selsing model, in this particular case of BS2 GCs, they increase with spherulite radius because the crystallized fraction inside each spherulite is higher for larger spherulites.

4.1.2. Biaxial strength

Fig. 10 shows that GCs containing spherulites with sizes of 5 and 10 μm lead to almost the same variation of σ_S as a function of f. In contrast, GCs with 30 and 100 μm spherulites, for $f = 20\%$ and 35%, showed σ_S values lower than that of the glass. For $f > 50\%$, σ_S increases with f, and it is higher than that in the GCs with 5 and 10 μm crystals. Spontaneous microcracking was observed in samples with 30 and 100 μm spherulites, as displayed in the insets of Fig. 10(a), and reduced the biaxial strength of the GCs. However, no microcracking was observed for the GC with 5 and 10 μm spherulites. This remark explains the difference in the variation of σ_S with f for the two groups (5–10 μm and 30–100 μm). For the GC with 30 μm spherulites, the increase in strength with f and its higher strength in relation to the GCs with 5 and 10 μm spherulites (for $f > 50\%$) are associated with its higher K_{IC}, as shown in Fig. 11(a).

Lange [33] measured the fracture strength of sodium borosilicate glass-alumina composites for particle sizes of 3.5, 11 and 44 μm, and for alumina volume fractions ranging from 10% to 40% using four-point bending tests. He observed that the fracture strength increased continuously with alumina volume fraction for the 3.5 and 11 μm particle sizes. For the composite with 44 μm particles, the strength decreased by approximately 30% in relation to the samples with 10% and 25% volume fractions (probably due to microcracking) and increased by 40% for $f = 40\%$.

Senk [34] studied the fracture strength of stoichiometric LS2 GCs using B3B tests. The crystallized volume fraction varied from 4% to 98% for three constant crystal sizes, from 7 to 30 μm. The glass flexural strength was 117 MPa, and increased up to 2.5 times for a crystallized volume fraction of 95%. Additionally, she observed that GC samples with the same f, but with smaller crystals have higher fracture strength.

High-strength glass-ceramics have been obtained by the crystallization of phases having higher thermal expansion coefficients than the residual glass, inducing high tensile thermal stresses in the crystals. For

instance, Wange et al. [35] reported an indentation fracture "toughness" of 4.3 MPa.m$^{1/2}$ for MgO-Al_2O_3-TiO_2-SiO_2 glass-ceramics where the β-quartz solid solution was crystallized and on cooling, the β- to α-quartz solid solution transition was observed. This transition causes a reduction in the crystal volume that, together with the large thermal expansion of α-quartz solid solution, yielded large thermal stresses.

In another work, Gawronski and Rüssel [36] observed very high fracture strengths, up to 450 MPa, in MgO-Y_2O_3-Al_2O_3-SiO_2-ZrO_2 glass-ceramics. For the sample without Y_2O_3, the main crystallized phase was the α-quartz solid solution observed at room temperature that underwent the β- to α- transition on cooling. Increasing Y_2O_3, the crystallization of quartz solid solution decreased and ZrO_2 was the main crystallized phase with acicular form of approximately 1 μm in length. This remarkable strength was attributed to the crystallization of tetragonal zirconia, with a much higher coefficient of thermal expansion than the base glass.

Strength measurements have also been made in liquid/liquid phase separated glasses with variable TEC mismatches. Utsumi et al. [37] measured the strength of Li and Na-borosilicate glasses. They observed for both glasses that the fracture strength decreases with increasing size of the dispersed glassy particles, proportional to d$^{-1/2}$ for a constant volume fraction. For the Li-borosilicate glass the 3-point bending strength decreased from 500 MPa for the pristine glass to 330 MPa for droplets of 180 nm. For the Na-borosilicate and the same droplet size, the strength decreased from 1050 MPa (pristine glass) to 470 MPa. In both cases, the TEC of the particles was higher than those of the matrix. These very high strengths are likely due to the chemical etching that reduced the size and amount of surface flaws, however in both cases, the strengths of the phase-separated glasses were smaller than those of the pristine (LPS-free glasses). Hence, in this case, LPS had a deleterious effect on strength.

Yet on liquid phase separated glasses, Häßler and Rüssel [38] determined that for a Na-borosilicate glass, the maximum strength correlated with the maximum tensile thermal residual stresses in the glassy particles. The highest strength was achieved for 70 nm particles. For smaller or greater particles, the strength decreased. Hence, these results are opposite to those of Utsumi et al. [37].

Much older revealing studies on strength versus residual stresses were performed for glass matrix composites (GMC) [39–42] (please note GMC are not glass-ceramics). In these works, the glass matrix chemical composition was varied to yield different TCEs - higher, equal, and lower than that of the particles – whereas the particle diameters and volume fractions were kept constant. For the largest particles, microcracking due to the thermal residual stresses was observed for glass matrixes with higher and lower TEC than the particles. In this case, the strength was maximum when the particle and the glassy matrix TCEs matched. The results were observed for alumina and Ni particles. For small particles, where no microcracking was observed, there was no conclusive result if residual stresses improved or decreased fracture strength, this is the reason why this is a relevant topic that warrants further research.

Another method to achieve high mechanical strength via residual compressive stresses is by surface crystallization of a low thermal expansion glass-ceramic. Seidel et al. [43] reported the crystallization of indialite in MgO-Al_2O_3-SiO_2 glass-ceramics. Indialite has a very low thermal expansion coefficient, $< 2.10^{-6}$ K^{-1}, and induces high compressive thermal stresses on the specimen surface. Fracture strengths as high as 1 GPa have been achieved. On the same line, in a recent study, Fabris et al. [44] achieved strengths of 680 MPa in translucent Li_2O-Al_2O_3-SiO_2 glass-ceramic having low TEC β-spodumene crystals on the glass surface.

If we assume that the critical defect is a semicircular crack with radius c at the surface, then $c = (K_{IC}/1.28\sigma_S)^2$ [45], where K_{IC} is the critical stress intensity factor for a particular spherulite volume fraction. If we assume that the critical defect occurs in the glass - the weaker phase, it is expected that fracture strength will increase with increasing f because of the diminishing distance between the spherulites and the increase in fracture toughness. The mean free path λ is a good estimator of the distance between spherulites and is given as $\lambda = 2d(1-f')/3f'$ [46,47], where d is the spherulite diameter. Fig. 14(a) shows the calculated c and λ as a function of f for the different spherulite sizes. In all cases, the critical defect size is larger than λ. This result is opposite to that of Serbena et al. [8] for LS2 GCs, where $c < \lambda$ for all crystallized volume fractions, which is likely due to the existence of residual glass inside the spherulites. GCs with 5 and 10 μm spherulites have the same mean free path because of the similar variation of σ_S and K_{IC}, but the 30 μm GCs have λ with a maximum at 20% and 35% as a result of spontaneous microcracking, as observed in the inset of Fig. 10(a).

Hasselman and Fulrath [47] proposed that, at low volume fractions, the average critical defect size is constant and does not depend on f. At higher volume fractions, the average defect size is governed by the mean distance between the inclusions, which is a function of both the volume fraction and the size of the inclusions. Fig. 14(b) shows the variation of σ_S as a function of $K_{IC}/\sqrt{\lambda}$. For GCs with sizes of 5 and 10 μm, there is a small increase, indicating that for these spherulite sizes, σ_S depends weakly on λ, and this small increase is related to the small increase in K_{IC} with f. For GCs with sizes of 30 and 100 μm, a linear dependence is observed, indicating that for these GCs, σ_S depends only on λ.

The reason for the different dependencies of σ_S as a function of $K_{IC}/\sqrt{\lambda}$might be that, for a constant spherulite volume fraction and small size, spherulites are dispersed in large numbers in the glass matrix, λ is smaller, and the interaction of the initial critical flaw with the

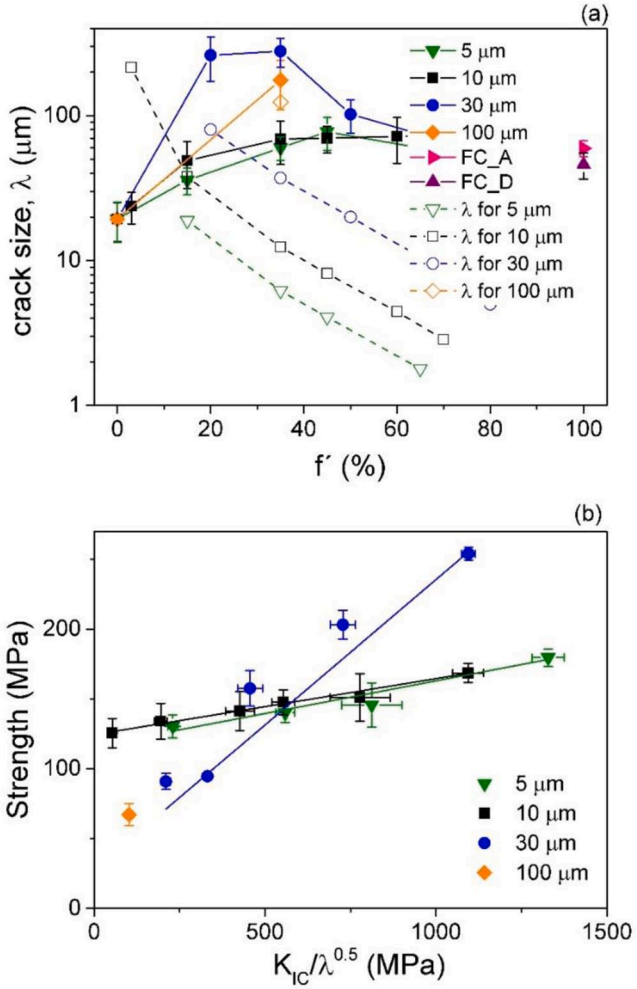

Fig. 14. (a) Critical crack size and mean free path between spherulites as a function of f and (b) variation of strength as a function of $K_{IC}/\lambda^{0.5}$ for different spherulite sizes. The lines are the best linear fits for each set of data.

spherulites is weak. For the same *f* and larger spherulites, there will be fewer spherulites in the matrix, the mean free path will be larger, and the spherulites will be more efficient in blocking the size of the critical defect. The higher blocking efficiency is related to the higher crystallized volume fractions of the 30 μm precipitates, as demonstrated in Fig. 6(a).

4.1.3. Fracture toughness

Results for BS2 GC regarding the variation of K_{IC} with *f* (Fig. 11(a)) and the amount of internal crystallization of the different spherulites (Fig. 6(b)) show that: a) spherulite size does not affect K_{IC}. Samples with spherulites with sizes of 5 and 10 μm have the same crystallized volume fraction and, despite the different crystal sizes, the same fracture toughness variation with *f*; b) residual stresses do not increase K_{IC}. Samples with higher K_{IC} were those with 30 μm spherulites, but these samples presented microcracking that relived the residual stresses; c) the higher K_{IC} of samples with 30 μm spherulites is due to the higher internal crystallization degree of their spherulites.

Serbena et al. [8] observed several toughening mechanisms in LS2 GCs: crack deflection, crack bowing, crack bridging and trapping, and a tougher crystalline phase. Higher internal crystallization of the spherulites means that crack bowing and crack bridging and trapping are more effective in increasing K_{IC}. The higher the spherulite internal crystallized degree, the tougher and stronger the spherulite, making it more difficult for a crack to penetrate the spherulites. In this case, crack pinning by this spherulite type is more effective than by spherulites having a lower degree of internal crystallization. Also, once a crack contours a spherulite, the spherulite bridges the crack surfaces behind. The higher its internal crystallization degree, the more effective the bridging.

Crack deflection can be estimated by the model proposed by Faber and Evans [29] and modified by Kotoul et al. [48]. Based on the experimental crack deflection angular distribution, it is possible to estimate its contribution to fracture toughness [8]. From the measurements of crack deflection distributions from Fig. S2, we can estimate the contribution of crack deflection to K_{IC}. The increase in toughening G_C due to crack deflection is given by [48]:

$$G_C = \frac{G_{Im}}{\langle G \rangle} G_{mc}, \tag{7}$$

where G_{mc} is the critical energy release rate of the glass and:

$$\frac{G}{G_{\mathrm{Im}}} = \cos^2\frac{\lambda}{2}\left(2\nu\sin^2\phi + \cos^2\frac{\lambda}{2}\right)^2\cos^4\phi + \cos^2\phi\sin^2\frac{\lambda}{2}\cos^4\frac{\lambda}{2} + \frac{\cos^2\frac{\lambda}{2}\sin^2\phi\cos^2\phi}{1-\nu}\left(2\nu + \cos^2\frac{\lambda}{2}\right)^2 \tag{8}$$

where λ and ϕ are the tilt and twist angles, respectively. We assumed that the angle distribution functions P_V for λ and ϕ are the same. Therefore, from the pseudo-Voigt functions fitted to the experimental data in Fig. S2, we calculated the increase in toughness as:

$$\frac{\langle G \rangle}{G_m} = \frac{\int_{-\frac{\pi}{2}}^{\frac{\pi}{2}}\int_{-\frac{\pi}{2}}^{\frac{\pi}{2}} P_V(\lambda)P_V(\phi)\frac{G}{G_m}d\lambda.d\phi}{\int_{-\frac{\pi}{2}}^{\frac{\pi}{2}}\int_{-\frac{\pi}{2}}^{\frac{\pi}{2}} P_V(\lambda)P_V(\phi)d\lambda.d\phi}, \tag{9}$$

The integrals were calculated numerically: $K_{IC}/K_{mIC} = \sqrt{G_C/G_{mC}}$ and the results are plotted in Fig. 15. The contribution of crack deflection to fracture toughness is not significant. The predicted contributions for samples with spherulite sizes of 5 and 30 μm are negligible. For the 10 μm GCs, the contribution is ~40%, and there is good agreement for the 100 μm GC. A close observation of Fig. 13(b) and 13(d) reveals that the crack deflection is higher in regions corresponding to where the crack cuts through the spherulites. Among other factors, crack path is affected by: a) difference in the elastic constants between the glass and the crystal, b) the residual stresses in the crystals and in the glass matrix,

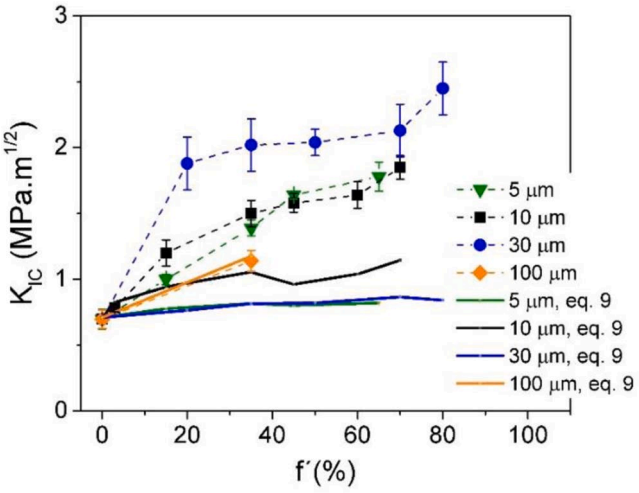

Fig. 15. Contribution of crack deflection to fracture toughness. Experimental and calculated fracture toughness values using Eq. (9) from the experimental crack deflection angle distribution are plotted as symbols and solid curves, respectively. The dashed lines are straight lines connecting the experimental points.

and c) the fracture toughness of the glass and precipitates. The first factor was modelled by He and Hutchinson [49] considering a crack approaching an interface joining two dissimilar materials. If the crack approaches a more compliant material across the interface, it will move towards the interface. If it approaches a stiffer material, it will curve away from the interface. The second factor was studied by He, Evans and Hutchinson [50] considering a crack approaching an interface of two dissimilar materials and subjected to residual stresses. If the crack approaches a material subjected to compressive stresses, penetration across the interface is favored, whereas tensile stresses favor deflection.

The third factor is that a crack tends to propagate in the material with lower toughness. In glass-ceramics, the crystals are usually stiffer than the glass matrix, favoring crack deflection. According to some authors, the type of residual stresses in the glass matrix could also affect the crack propagation path and the material toughness [32,51]. Hence, this is a relevant topic, worth of further investigation. Compressive residual stresses in the crystal induce compressive radial stress and tensile hoop stresses in the glass matrix, favoring propagation towards the crystals, whereas tensile residual stresses in the crystal induce tensile radial stress and compressive hoop stresses in the glass matrix, favoring deflection away from crystals [5]. Also, crystals are normally tougher than glasses. In BS2 GCs, the spherulites are no more than 20% stiffer than the residual glass (Fig. 8b), indicating that a crack does not have a strong tendency to deviate from them. Tensile residual stresses in the spherulites with 5 and 10 μm sizes also favor crack deflection from the spherulites. The higher K_{IC} of the spherulites (Fig. 10a) also favors crack propagation along the glass/spherulite interface, and not inside the spherulites.

Residual stresses caused microcracking in the GCs with 30 and 100 μm spherulites. The measured residual stresses shown in Fig. 9 are null when microcracking is present. Therefore, the residual stress does not influence the K_{IC} of these samples. In this same topic, Villas-Boas et al. [52] varied the magnitude of residual stress in LS2 GCs by varying the TECs of the residual glass, and also found no evidence for a residual stress effect on K_{IC}.

A related study was carried out with LS2 GCs that show compressive stresses in the crystals, while the current BS2 samples show tensile stresses in the crystals. It is interesting to note that for the almost fully crystallized GCs, both systems showed fracture toughness values close to 3.5 MPa.m$^{1/2}$ (Fig. 11(b)), corroborating the previous discussion that residual stresses of this level (40–170 MPa) in the crystals do not

significantly affect K_{IC}. Hence, we also expect no effect of residual stress in the 5 and 10 μm GCs. Finally, microcracking of the 30 and 100 μm GCs have not affected fracture toughness. The highest K_{IC} was observed for the 30 μm GCs, which have the highest crystallized volume fractions inside the spherulites, as shown in Fig. 6(b). The lower K_{IC} of the samples with 100 μm spherulites may be due to the lower crystallization of their spherulites, as also displayed in Fig. 6(a).

On this same topic, Lange [33] measured the fracture toughness of sodium borosilicate glass-alumina composites with three different particle sizes: 3.5, 11 and 44 μm, and three different volume fractions: 10%, 25% and 40%. He found that the higher the volume fraction and particle size, the higher the K_{IC}. A close inspection of the fracture surfaces indicated that, for the 3.5 and 11 μm particle size composites, the cracks interacted with the particles and propagated around most of them, whereas for the 44 μm composite samples, the crack crossed most of the polycrystalline alumina particles. Alumina is known to present R-curve behavior [53] and, as a crack cuts through the larger 44 μm particles, these composites present improved fracture toughness but lower fracture strength. Lange's results are similar to ours. The 30 μm GCs presented the lowest strength for low f and the largest K_{IC}. The R-curve behavior mechanism may also be operative, to some extent, in our samples, since the 30 μm GCs presented the highest crystallized volume fraction inside the spherulite and the second largest crystals.

Evidence of higher fracture toughness for GCs with larger crystal sizes was also shown in [54], where a GC with a 50% volume of plate-like metasilicate crystals with sizes in the 5–25 μm range presented a K_{IC} of 3.5 ± 0.5 MPa.m$^{1/2}$. Another study [55] on GCs with LS2 crystals < 50 nm and crystallized volume fractions of 52% LS2 and 26% LS crystals presented a lower indentation crack resistance of 1.0 ± 0.1 MPa.m$^{1/2}$. Commercial dental LS2 glass-ceramics that have a microstructure with 2–5 μm lath LS2 crystals and a 50–70% crystallized volume fraction present fracture toughness in the range of 1.5–3.3 MPa.m$^{1/2}$ [54,56–62].

Senk studied the fracture toughness of LS2 GCs as a function of crystallized volume fraction for three crystal sizes (8, 13 and 34 μm), using the four-point bending technique, and observed an increase in the crystallized volume fraction and that the larger the grain size, the greater the K_{Ic} [34]. For the glassy sample, the fracture toughness was 0.8 ± 0.1 MPa.m$^{1/2}$, whereas for a GC with 34 μm crystals and volume fraction 80%, it was 3.1 ± 0.2 MPa.m$^{1/2}$, i.e., a 280% increase over that of the glass.

Freiman et al. [63] observed that the flexural strength decreased with spherulite size, and both flexural strength and fracture toughness increased with spherulite volume fraction for B3S5 GCs. Microcracking was observed for samples heat-treated at temperatures > 1000 °C. Hill et al. [64] measured the fracture strength and fracture toughness of B3S5 GCs with three crystal sizes (from 1.5 to 15 μm) and 70–80% crystallized volume fractions. The fracture strength and toughness increased with both crystal size and aspect ratio. Moriceau et al. [65] observed that fracture toughness increased with spherulite volume fraction, and spontaneous microcracking was also observed in B2S3 GCs. Lubauer et al. [66] measured the K_{IC} of several commercial lithium-based GCs, and observed that the fracture toughness values of GCs with nanometric crystals were lower than those of GCs with crystals > 1 μm.

Therefore, enough experimental evidence indicates that the larger the crystal size and the crystallized volume fraction, the larger the fracture toughness in glass-ceramics. This seems to be the most important factor for any tough glass-ceramic. It is also relevant to note that if K_{IC} is plotted against the crystallized volume fraction, all data fall on the same curve, except for the 100 μm GC (that microcracked), which indicates that the crystallized volume fraction of a tougher phase is a fundamental feature controlling fracture toughness in BS2 GCs, which show tensile residual stresses. The same behavior was observed in our previous study for LS2 GCs [8] showing compressive residual stresses in the crystals.

5. Summary and conclusions

This is a systematic work on the mechanical properties of glass-ceramics containing crystals subjected to *tensile* internal residual stresses. We evaluated the effects of the microstructure and residual stresses on the fracture strength and toughness by *independently* varying the crystallized fraction and the grain size. This work on BS2 GCs containing crystals under tensile residual stresses differs from two previous studies on glass-ceramics that also varied the crystallized fraction and grain size independently because they focused on crystals under *compressive* residual stresses.

The spherulitic crystals in these GCs are composed of dendrites and axialites with some residual glass between the crystal arms. Due to *tensile* residual stresses, samples with any crystallized volume fraction spontaneously fractured for spherulite diameters ≥ 30 μm. The amount of residual glass inside the spherulites decreases with longer heat treatments, higher temperatures, and larger spherulite sizes. For GCs containing small (5 and 10 μm) uncracked spherulites, the fracture strength increases with spherulite volume fraction and depends weakly on the mean free path, λ, between crystals. However, for GCs with large (30 and 100 μm) splintered spherulites, the fracture strength depends strongly on λ. This dependence is due to the higher crystallized volume fraction inside these larger spherulites in relation to the smaller spherulites. For GCs with spherulites > 30 μm and f <30%, the fracture strength was lower than that of the parent glass because of microcracking.

In general, fracture toughness increased with spherulite size and volume fraction. Spherulites showing higher degrees of internal crystallization led to crack bowing, bridging and trapping, which were effective in increasing fracture toughness. The higher toughness of the 30 μm GCs is related to the higher crystallized fraction inside the spherulites, which causes sturdier crack interaction with them and possibly leads to R-curve behavior.

An important observation is that the dependence of K_{IC} with the GC crystallized volume fraction is the *same* for all these barium silicate GCs having different grain sizes, in which the crystals are under *tensile* internal residual stresses of 40–170 MPa.

Yet on this matter, it is quite significant that lithium silicate glass-ceramics showing crystals under *compressive* residual stress of − 65 MPa show a very similar tendency with the volume fraction crystallized. These combined results for two glass-ceramic families indicate that the residual stress *type is not* relevant and that the crystallized volume fraction of a tougher phase is the crucial microstructural feature controlling the fracture toughness of GCs. Therefore, our discoveries with BS2, with tensile internal residual stresses, combined with our previous work on a GC with crystals under compressive residual stress, shed light on unknown aspects of microstructure-residual stress-property behavior and can be quite useful to design novel strong and tough glass-ceramics.

Declaration of Competing Interest

The authors declare that they have no known competing financial interests or personal relationships that could have appeared to influence the work reported in this paper.

Acknowledgements

The authors would like to thank the Brazilian development agencies CAPES, CNPq, FINEP, Fundação Araucária, and UGF/PR for their financial support. We are also grateful to Dr. Benjamin J. A. Moulton for the EPMA analysis. The C-LABMU/ UEPG and C2MMA LabMult/UTFPR provided research facilities. This study used resources under proposal 20160222 of the Brazilian Synchrotron Light Laboratory (LNLS), an open national facility operated by the Brazilian Center for Research in Energy and Materials (CNPEM). The São Paulo Research Foundation

(FAPESP), process no. 2013/07793-6 (CEPID), also contributed to funding this study. Finally, we are indebted to Profs. J.J. Mecholsky Jr. and U. Lohbauer for their valuable critical comments.

Appendix A. Supporting information

Supplementary data associated with this article can be found in the online version at doi:10.1016/j.jeurceramsoc.2022.05.073.

References

[1] J. Deubener, M. Allix, M.J. Davis, A. Duran, T. Höche, T. Honma, T. Komatsu, S. Krüger, I. Mitra, R. Müller, S. Nakane, M.J. Pascual, J.W.P. Schmelzer, E. D. Zanotto, S. Zhou, Updated definition of glass-ceramics, J. Non Cryst. Solids 501 (2018) 3–10, https://doi.org/10.1016/j.jnoncrysol.2018.01.033.

[2] O. Peitl, E.D. Zanotto, F.C. Serbena, L.L. Hench, Compositional and microstructural design of highly bioactive P2O5-Na2O-CaO-SiO2glass-ceramics, Acta Biomater. 8 (2012) 321–332, https://doi.org/10.1016/j.actbio.2011.10.014.

[3] F.C. Serbena, G.P. Souza, E.D. Zanotto, J. Lumeau, L. Glebova, L.B. Glebov, Internal residual stresses in partially crystallized Photo-Thermo-Refractive glass, J. Am. Ceram. Soc. 94 (3) (2011) 671–674, https://doi.org/10.1111/j.1551-2916.2010.04372.x.

[4] E.D. Zanotto, A bright future for glass-ceramics, Am. Ceram. Soc. Bull. 89 (2010) 19–27.

[5] F.C. Serbena, E.D. Zanotto, Internal residual stresses in glass-ceramics: a review, J. Non Cryst. Solids 358 (2012) 975–984, https://doi.org/10.1016/j.jnoncrysol.2012.01.040.

[6] E.D. Zanotto, The Effects of Amorphous Phase Separation on Crystal Nucleation in Baria-Silica and Lithia-Silica Glasses, University of Sheffield, Inglaterra, 1982.

[7] S.B. Massardo, Nanoindentação em Vitocerâmicas de Dissilicato de Lítio-Fractografia e Propriedades Mecânicas, Universidade Federal do Paraná,, 2011.

[8] F.C. Serbena, I. Mathias, C.E. Foerster, E.D. Zanotto, Crystallization toughening of a model glass-ceramic, Acta Mater. 86 (2015) 216–228, https://doi.org/10.1016/j.actamat.2014.12.007.

[9] S.E. Braun, A. Mikowski, A.N. Comin, L.A. Thesing, P. Soares, Influence of crystallization on hardness, elastic modulus and fracture toughness in lithium disilicate Li2O.2SiO2 glass-ceramics, Cerâmica 64 (2018) 301–310, https://doi.org/10.1590/0366-69132018643702312.

[10] A.M. Rodrigues, D.R. Cassar, V.M. Fokin, E.D. Zanotto, Crystal growth and viscous flow in barium disilicate glass, J. Non Cryst. Solids 479 (2018) 55–61, https://doi.org/10.1016/j.jnoncrysol.2017.10.007.

[11] A.A. Coelho, TOPAS and TOPAS-Academic: an optimization program integrating computer algebra and crystallographic objects written in C ++, J. Appl. Crystallogr. 51 (2018) 210–218, https://doi.org/10.1107/S1600576718000183.

[12] E.D. Zanotto, P.F. James, Experimental test of the general theory of transformation kinetics: Homogeneous nucleation in a BaO.2SiO2 glass, J. Non Cryst. Solids 104 (1988) 70–72, https://doi.org/10.1016/0022-3093(88)90183-4.

[13] W.C. Oliver, G.M. Pharr, An improved technique for determining hardness and elastic modulus using load and displacement sensing indentation experiments, J. Mater. Res. Soc. 7 (1992) 1564–1583, https://doi.org/10.1557/JMR.1992.1564.

[14] R. Danzer, W. Harrer, P. Supancic, T. Lube, Z. Wang, A. Börger, The ball on three balls test-strength and failure analysis of different materials, J. Eur. Ceram. Soc. 27 (2007) 1481–1485, https://doi.org/10.1016/j.jeurceramsoc.2006.05.034.

[15] J.J. Swab, J. Tice, A.A. Wereszczak, R.H. Kraft, Fracture toughness of advanced structural ceramics: applying ASTM C1421, J. Am. Ceram. Soc. 15 (2014) 1–9, https://doi.org/10.1111/jace.13293.

[16] J.J. Swab, J. Tice, A.A. Wereszczak, R.H. Kraft, Fracture toughness of advanced structural ceramics: applying ASTM C1421, J. Am. Ceram. Soc. 98 (2015) 607–615, https://doi.org/10.1111/jace.13293.

[17] R. Morrell, Fracture toughness testing for advanced technical ceramics: internationally agreed good practice, Adv. Appl. Ceram. 105 (2006) 88–98, https://doi.org/10.1179/174367606×84422.

[18] L.A. Silva, J.M.R. Mercury, A.A. Cabral, Determining the crystal volume fraction of BS2 glass by differential scanning calorimetry and optical microscopy, J. Am. Ceram. Soc. 96 (2013) 130–136, https://doi.org/10.1111/jace.12097.

[19] A.H. Ramsden, P.F. James, The effects of amorphous phase separation on crystal nucleation kinetics in BaO-SiO2 glasses - part 1 General survey, J. Mater. Sci. 19 (1984) 1406–1419.

[20] B.J.A. Moulton, A.M. Rodrigues, D.V. Sampaio, L.D. Silva, T.R. Cunha, D. Zanotto, P.S. Pizani, The origin of the unusual DSC peaks of supercooled barium disilicate liquid, CrystEngComm (2019) 2768–2778, https://doi.org/10.1039/C8CE02054J.

[21] B.J.A. Moulton, S.R.F. Sabino, L.L. Evaristo, V. Sampaio, S. Buchner, F.C. Serbena, P.S. Pizani, E.D. Zanotto, Unusual crystallization pathways of six barium disilicate glasses, in preparation (2022).

[22] S. Rodríguez-López, J. Wei, K.C. Laurenti, I. Mathias, V.M. Justo, F.C. Serbena, C. Baudín, J. Malzbender, M.J. Pascual, Mechanical properties of solid oxide fuel cell glass-ceramic sealants in the system BaO/SrO-MgO-B2O3-SiO2, J. Eur. Ceram. Soc. 37 (2017) 3579–3594, https://doi.org/10.1016/j.jeurceramsoc.2017.03.054.

[23] M. Kerstan, C. Rüssel, Barium silicates as high thermal expansion seals for solid oxide fuel cells studied by high-temperature X-ray diffraction (HT-XRD), J. Power Sources 196 (2011) 7578–7584, https://doi.org/10.1016/j.jpowsour.2011.04.035.

[24] L.A. Gorelova, R.S. Bubnova, S.V. Krivovichev, M.G. Krzhizhanovskaya, S. K. Filatov, Thermal expansion and structural complexity of Ba silicates with tetrahedrally coordinated Si atoms, J. Solid State Chem. 235 (2016) 76–84, https://doi.org/10.1016/j.jssc.2015.12.012.

[25] M.E. Broz, R.F. Cook, D.L. Whitney, Microhardness, toughness, and modulus of Mohs scale minerals, Am. Mineral. 91 (2006) 135–142, https://doi.org/10.2138/am.2006.1844.

[26] A.C. Larson, R.B.V. Dreele, (GSAS) - General Structure Analysis System, Https://Subversion.Xor.Aps.Anl.Gov/EXPGUI/Gsas/All/GSAS.Manual.Pdf. (2004) 224.

[27] N. Soga, H. Yamanaka, C. Hisamoto, M. Kunugi, Elastic properties and struture of alkaline-earth silicate glasses, J. Non Cryst. Solids 22 (1976) 67–76, https://doi.org/10.1016/0022-3093(76)90008-9.

[28] ⟨https://materialsproject.org/materials/mp-3031/⟩, (n.d.). https://materialsproject.org/materials/mp-3031/ (Accessed 27 April 2021).

[29] K.T. Faber, A.G. Evans, Crack deflection processes - I. Theory, Acta Met. 31 (1983) 565–576, https://doi.org/10.1016/0001-6160(83)90046-9.

[30] J. Selsing, Internal Stresses in Ceramics, J. Am. Ceram. Soc. 44 (1961), https://doi.org/10.1111/j.1151-2916.1961.tb15475.x.

[31] F.C. Serbena, V.O. Soares, O. Peitl, H. Pinto, R. Muccillo, E.D. Zanotto, Internal residual stresses in sintered and commercial low expansion Li2O-Al2O3-SiO2 Glass-Ceramics, J. Am. Ceram. Soc. 94 (2011) 1206–1214, https://doi.org/10.1111/j.1551-2916.2010.04220.x.

[32] R.W. Davidge, T.J. Green, The strength of two-phase ceramic/glass materials, J. Mater. Sci. 3 (1968) 629–634, https://doi.org/10.1007/bf00757910.

[33] F.F. Lange, Fracture energy and strength behavior of a sodium borosilicate glass-Al2O3 composite system, J. Am. Ceram. Soc. 54 (1971) 614–620, https://doi.org/10.1111/j.1151-2916.1971.tb16016.x.

[34] M.V. Senk, Efeito da fração cristalina e tamanho de cristal na resistência mecânica e tenacidade a fratura da vitrocerâmica de dissilicato de litio, Universidade Estadual de Ponta Grossa, 2017.

[35] P. Wange, T. Höche, C. Rüssel, J.D. Schanapp, Microstructure-property relationship in high-strength MgO–Al2O3–SiO2–TiO2 glass-ceramics, J. Non-Cryst. Solids 298 (2002) 137–145, https://doi.org/10.1016/S0022-3093(02)00950-X.

[36] A. Gawronski, C. Rüssel, High strength glass-ceramics in the system MgO/Y2O 3/Al2O3/SiO2/ZrO2 without quartz as crystalline phase, J. Mater. Sci. 48 (2013) 3461–3468, https://doi.org/10.1007/s10853-013-7136-9.

[37] Y. Utsumi, S. Sakka, M. Tashiro, Experimental study on the bending strength of glass in relation to liquid-liquid phase separation, Glass Technol. 11 (1970) 80–85.

[38] J. Häßler, C. Rüssel, Effect of microstructure of a phase separated sodium-borosilicate glass on mechanical properties, Ceram. Int. 43 (2017) 11403–11409, https://doi.org/10.1016/j.ceramint.2017.05.349.

[39] F.F. Lange, Fracture of brittle matrix, particulate composites, in: L.J. Broutman (Ed.), Fracture and Fatigue, Academic Press, New York (USA), 1974, pp. 1–44.

[40] W.J. Frey, J.D. Mackenzie, Mechanical properties of selected glass-crystal composites, J. Mater. Sci. 2 (1967) 124–130, https://doi.org/10.1007/BF00549571.

[41] M.A. Stett, R.M. Fulrath, Mechanical properties and fracture behavior of chemically bonded composites, J. Am. Ceram. Soc. 53 (1970) 5–13, https://doi.org/10.1111/j.1151-2916.1970.tb11989.x.

[42] D.B. Binns, Some physical properties of two-phase crystal glass-solids, in: G. H. Stewart (Ed.), Science of Ceramics, Academic Press, New York, 1962, pp. 315–335.

[43] S. Seidel, M. Dittmer, W. Wisniewski, W. Höland, C. Rüssel, Effect of the ZrO2 concentration on the crystallization behavior and the mechanical properties of high-strength MgO–Al2O3–SiO2 glass–ceramics, J. Mater. Sci. 52 (2016) 1955–1968, https://doi.org/10.1007/s10853-016-0484-5.

[44] D.C.N. Fabris, E.H. Miguel, R. Vargas, R.B. Canto, M. de, O. Carlos Villas Boas, O. Peitl, V.M. Sglavo, E.D. Zanotto, Microstructure, residual stresses, and mechanical performance of surface crystallized translucent glass-ceramics, J. Eur. Ceram. Soc. 42 (2022) 4631–4642, https://doi.org/10.1016/j.jeurceramsoc.2022.04.024.

[45] J.C. Newman, I.S. Raju, An empirical stress-intensity factor equation for the surface crack, Eng. Fract. Mech. 15 (1981) 185–192, https://doi.org/10.1016/0013-7944(81)90116-8.

[46] D.J. Green, Fracture toughness predictions for crack bowing in brittle particulate composites, Commun. Am. Ceram. Soc. 66 (1983) C-4–C-5, https://doi.org/10.1111/j.1151-2916.1983.tb09975.x.

[47] D.P.H. Hasselman, R.M. Fulrath, Proposed fracture theory of a dispersion-strengthened glass matrix, J. Am. Ceram. Soc. 49 (1966) 68–72, https://doi.org/10.1111/j.1151-2916.1966.tb13210.x.

[48] M. Kotoul, J. Pokluda, P. Šandera, I. Dlouhý, Z. Chlup, A.R. Boccaccini, Toughening effects quantification in glass matrix composite reinforced by alumina platelets, Acta Mater. 56 (2008) 2908–2918, https://doi.org/10.1016/j.actamat.2008.02.024.

[49] H. Ming-Yuan, J.W. Hutchinson, Crack deflection at an interface between dissimilar elastic materials, Int. J. Solids Struct. 25 (1989) 1053–1067, https://doi.org/10.1016/0020-7683(89)90021-8.

[50] H. Ming-Yuan, Anthony G. Evans, J.W. Hutchinson, Crack deflection at an interface between dissimilar elastic materials:role of residual stresses, Int. J. Solids Struct. 31 (1994) 3443–3455, https://doi.org/10.1016/0020-7683(94)90025-6.

[51] H. Cai, N.P. Padture, B.M. Hooks, B.R. Lawn, Flaw tolerance and toughness curves in two-phase particulate composites: SiC/glass system, J. Eur. Ceram. Soc. 13 (1994) 149–157, https://doi.org/10.1016/0955-2219(94)90113-9.

[52] M.O.C. Villas-Boas, F.C. Serbena, V.O. Soares, I. Mathias, E.D. Zanotto, Residual stress effect on the fracture toughness of lithium disilicate glass-ceramics, J. Am. Ceram. Soc. 103 (2019) 465–479, https://doi.org/10.1111/jace.16664.

[53] G. Vekinis, M.F. Ashby, P.W.R. Beaumont, R-curve behaviour of Al2O3 ceramics, Acta Metall. Mater. 38 (1990) 1151–1162, https://doi.org/10.1016/0956-7151(90)90188-M.
[54] V.O. Soares, F.C. Serbena, I. Mathias, M.C. Crovace, E.D. Zanotto, New, tough and strong lithium metasilicate dental glass-ceramic, Ceram. Int. 47 (2020) 2793–2801, https://doi.org/10.1016/j.ceramint.2020.09.133.
[55] V.O. Soares, F.C. Serbena, G. dos, S. Oliveira, C. da Cruz, R.F. Muniz, E.D. Zanotto, Highly translucent nanostructured glass-ceramic, Ceram. Int. 47 (2021) 4707–4714, https://doi.org/10.1016/j.ceramint.2020.10.039.
[56] IPS e.max Press, (n.d.). ⟨https://asia.ivoclarvivadent.com/en-as/all-products/ips-emax-press/⟩ (Accessed 27 April 2021).
[57] F. Zhang, H. Reveron, B.C. Spies, B. Van Meerbeek, J. Chevalier, Trade-off between fracture resistance and translucency of zirconia and lithium-disilicate glass ceramics for monolithic restorations, Acta Biomater. 91 (2019) 24–34, https://doi.org/10.1016/j.actbio.2019.04.043.
[58] R. Belli, M. Wendler, A. Petschelt, T. Lube, U. Lohbauer, Fracture toughness testing of biomedical ceramic-based materials using beams, plates and discs, J. Eur. Ceram. Soc. 38 (2018) 5533–5544, https://doi.org/10.1016/j.jeurceramsoc.2018.08.012.
[59] Macor Machinable glass-ceramic for industrial applications, (n.d.). ⟨https://www.corning.com/in/en/products/advanced-optics/product-materials/specialty-glass-and-glass-ceramics/glass-ceramics.html⟩ (accessed September 27, 2021).
[60] R. Belli, M. Wendler, J.I. Zorzin, U. Lohbauer, Practical and theoretical considerations on the fracture toughness testing of dental restorative materials, Dent. Mater. 34 (2018) 97–119, https://doi.org/10.1016/j.dental.2017.11.016.
[61] E. Homaei, K. Farhangdoost, J.K.H. Tsoi, J.P. Matinlinna, E.H.N. Pow, Static and fatigue mechanical behavior of three dental CAD/CAM ceramics, J. Mech. Behav. Biomed. Mater. 59 (2016) 304–313, https://doi.org/10.1016/j.jmbbm.2016.01.023.
[62] W. Höland, M. Schweiger, M. Frank, V. Rheinberger, A comparison of the microstructure and properties of the IPS Empress®2 and the IPS Empress® glass-ceramics, J. Biomed. Mater. Res. 53 (2000) 297–303, https://doi.org/10.1002/1097-4636(2000)53:4<297::aid-jbm3>3.0.co;2-g.
[63] S.W. Freiman, G.Y. Onoda, A.G. Pincus, Mechanical properties of 3Ba0 5SiO2 glass-ceramics, J. Am. Ceram. Soc. 57 (1974) 8–12, https://doi.org/10.1111/j.1151-2916.1974.tb11352.x.
[64] T.J. Hill, J.J. Mecholsky, K.J. Anusavice, Fractal analysis of toughening behavior in 3BaO5SiO2 glass-ceramics, J. Am. Ceram. Soc. 83 (2000) 545–552, https://doi.org/10.1111/j.1151-2916.2000.tb01232.x.
[65] J. Moriceau, P. Houizot, T. To, A. Mougari, H. Orain, F. Celarié, T. Rouxel, Nucleation and crystallization of Ba2Si3O8 spherulites in a barium aluminum silicate glass, and mechanical properties of the obtained glass-ceramics, J. Eur. Ceram. Soc. 41 (2021) 838–848, https://doi.org/10.1016/j.jeurceramsoc.2020.08.025.
[66] J. Lubauer, R. Belli, H. Peterlik, K. Hurle, U. Lohbauer, Grasping the Lithium hype: insights into modern dental Lithium Silicate glass-ceramics, Dent. Mater. 38 (2022) 318–332, https://doi.org/10.1016/j.dental.2021.12.013.